Composition can buffer protein dynamics within liquid-like condensates.

Stela Jelenic[1,2], Janos Bindics[1], Philipp Czermak[1], Balashankar R Pillai[1,2], Martine Ruer[3], Carsten Hoege[3], Alex S Holehouse[4], Shambaditya Saha[1,5]

[1]Institute of Molecular Biotechnology of the Austrian Academy of Sciences (IMBA), Vienna BioCenter (VBC), Dr. Bohr-Gasse 3, 1030 Vienna, Austria.

[2]Vienna BioCenter PhD Program, Doctoral School of the University of Vienna and Medical University of Vienna, 1030 Vienna, Austria.

[3]Max Planck Institute of Molecular Cell Biology and Genetics, 01307 Dresden, Germany.

[4]Department of Biochemistry and Molecular Biophysics, Washington University School of Medicine, St. Louis, MO 63110, USA.

[5]Correspondence: shambaditya.saha@imba.oeaw.ac.at

Summary

Most non-membrane-bound compartments in cells that form via phase separation have complex composition. Phase separation of individual proteins that form these compartments has been well documented. However, we know relatively little about how the dynamics of individual proteins are modulated in multicomponent systems. Here, we used in vitro reconstitution and in vivo experiments to investigate how complex composition within a liquid-like 'P granule' compartment affects the dynamics of one of its scaffold proteins PGL-3. Using mutational analysis and biophysical perturbations, we generated PGL-3 constructs with reduced alpha-helicity that phase separate in vitro into condensates with widely varying dynamics. We use these PGL-3 constructs to show that introducing other P granule components buffers against large change of dynamics within liquid-like compartments. This dynamics-buffering effect is mediated by weak interactions among two or more components. Such dynamics-buffering may contribute to robust functional output of cellular liquid-like compartments.

Introduction

To organize biochemistry, cells assemble compartments with distinct compositions. Many of these compartments are not enclosed within lipid membranes and assemble via liquid-liquid phase separation (LLPS) of proteins and RNAs from the surrounding cytoplasm or nucleoplasm (Banani *et al*, 2017; Brangwynne *et al*, 2009; Lyon *et al*, 2021). Studies over the past decade have focused on identifying the molecular mechanisms of LLPS within cells. The current model is that LLPS is driven by 'scaffold' proteins and/or RNAs which participate in homotypic or heterotypic interactions with each other to assemble cellular non-membrane-bound compartments (Van Treeck & Parker, 2018; Banani *et al*, 2016, 2017; Lyon *et al*, 2021; Riback *et al*, 2020; Sanders *et al*, 2020; Saha *et al*, 2016). Other macromolecules called 'clients' do not contribute to compartment assembly but concentrate within those compartments and modulate biological function. It is now appreciated that LLPS can be driven by interactions of different types i.e. electrostatic, polar or hydrophobic interactions involving both folded domains and intrinsically disordered regions (Banani *et al*, 2017; Lyon *et al*, 2021). The mechanisms that regulate dynamics of components within these compartments, however, remain unclear.

Macromolecules can phase separate into condensates with different material properties, ranging from liquid-like phases with fast dynamics to dynamically-arrested gels as well as glasses (Banani *et al*, 2017; Jawerth *et al*, 2020). Many liquid-like condensates *in vitro* have also been shown to mature over time, starting as liquid-like droplets that transition into non-dynamic assemblies (Banani *et al*, 2017). The rates of biochemical reactions within biomolecular condensates must depend on the diffusion times of the components. Recent *in vitro* investigations of LLPS for simple two-component systems have shown that the behavior of one component can modulate the dynamics of another within condensates (Boeynaems *et al*, 2019; Rhine *et al*, 2020; Zhang *et al*, 2015; Alshareedah *et al*, 2021). Cellular condensates contain hundreds of different proteins and RNAs (e.g. P granules, P bodies and stress granules (Youn *et al*, 2019; Phillips & Updike, 2022)). How such complex composition affects dynamics of macromolecules in liquid-like compartments remains poorly understood.

65 P granules are a canonical liquid-like compartment found in the germline of *C. elegans*
66 (Strome & Wood, 1982; Brangwynne *et al*, 2009). mRNA and over 70 proteins are known to
67 concentrate in P granules (Phillips & Updike, 2022). Mutations in P granule proteins are
68 associated with loss of fertility and fecundity in *C. elegans* (Phillips & Updike, 2022; Updike
69 & Strome, 2010). Eight proteins – PGL-1, PGL-3, GLH-1, GLH-2, GLH-3, GLH-4, DEPS-1
70 and MIP-1 are currently known to be constitutive P granule components i.e., these proteins
71 concentrate within P granules at all stages of germline development (Kawasaki *et al*, 1998,
72 2004; Spike *et al*, 2008a, 2008b; Price *et al*, 2021; Cipriani *et al*, 2021; Phillips & Updike,
73 2022). Proteins of the PGL family are specific to the *Caenorhabditis* genus and contain
74 RNA-binding motifs. The GLH- proteins belong to the highly conserved family of DEAD-box
75 RNA helicases. Based on current estimates of the concentrations of these proteins in vivo,
76 the PGL- and GLH- proteins are among the most abundant constitutive components in P
77 granules (Saha *et al*, 2016). In vitro reconstitution experiments have shown that, among the
78 constitutive P granule proteins, only the protein PGL-3 can phase separate into liquid-like
79 condensates in vitro (Saha *et al*, 2016, 201; Hanazawa *et al*, 2011). Two other proteins that
80 concentrate in P granules – MEG-3 and LAF-1 can also phase separate into liquid-like
81 condensates in vitro (Smith *et al*, 2016; Elbaum-Garfinkle *et al*, 2015). This suggests that
82 phase separation of these proteins also contribute to the assembly of P granules at some
83 stages of germline development. The interactions that support phase separation of the
84 PGL-3 protein remain unclear. Structural studies on the orthologous PGL-1 protein revealed
85 two dimerization domains (Aoki *et al*, 2016, 2021). This raises the possibility that PGL-3
86 also contains similar dimerization domains, and phase separation depends on interactions
87 involving these domains. The PGL-3 protein can phase separate in vitro only at high 'non-
88 physiological' protein concentrations (Saha *et al*, 2016). At physiological concentrations
89 (approx. 1 μM), binding to mRNA facilitates phase separation of the PGL-3 protein (Saha *et*
90 *al*, 2016). It remains unclear if interactions among the dimerization domains cooperate with
91 mRNA binding to support phase separation of the PGL-3 protein.
92
93 Here, we use in vitro reconstitution and in vivo experiments in adult *C. elegans* gonads to
94 investigate how complex composition within the P granule compartment contributes to the
95 dynamics of one of its scaffold proteins PGL-3 (Saha *et al*, 2016; Hanazawa *et al*, 2011).
96 We begin with structure-function analysis for insights into the mechanism of phase

separation of the PGL-3 protein. Using a combination of mutational analysis and biophysical perturbations, we generated PGL-3 constructs that phase separate in vitro into condensates with widely varying dynamics. Investigating the effect of other P granule components on phase separation of PGL-3 constructs, we uncovered a role of complex composition in buffering against large change of dynamics within cellular liquid-like compartments. This “dynamics-buffering” effect is distinct from active processes that depend on ATP hydrolysis, but is mediated by weak interactions among components in liquid-like compartments.

Results

Homotypic and heterotypic interactions drive phase separation of PGL-3 and mRNA at physiological concentrations.

We began by investigating the role of different domains in the phase separation properties of the protein PGL-3 in vitro (Supplementary Fig. 1). Together with other proteins and mRNA, PGL-3 drives the assembly of the canonical liquid-like P granules in the germline of *C. elegans*. Bioinformatic analysis of the 693 residue-long PGL-3 protein predicted that the N-terminus accounting for ~65% of PGL-3 is predominantly α-helical, while the C-terminus accounting for ~35% is mostly disordered (Fig. 1a, Supplementary Fig. 2a, 2b). Consistent with the bioinformatics predictions, circular dichroism (CD) spectroscopy under conditions that do not support phase separation showed that the PGL-3 N-terminal fragment 1-452 is predominantly α-helical, while the C-terminal fragment 370-693 is disordered (Fig. 1f).

Intrinsically disordered polypeptides have in many cases been shown to be necessary and sufficient to drive phase separation. We therefore tested if a recombinantly purified C-terminal fragment of PGL-3 (370-693), can drive phase separation in vitro. To our surprise, we did not observe any phase separation even at high protein concentrations up to ~70 μM (Fig. 1b, c). However, we found that a recombinantly purified N-terminal fragment of PGL-3 (1-452) phase separates into condensates at close to physiological concentrations of PGL-3 (Fig. 1b, c, Supplementary figure 2e). Similar to full-length PGL-3, condensates of the N

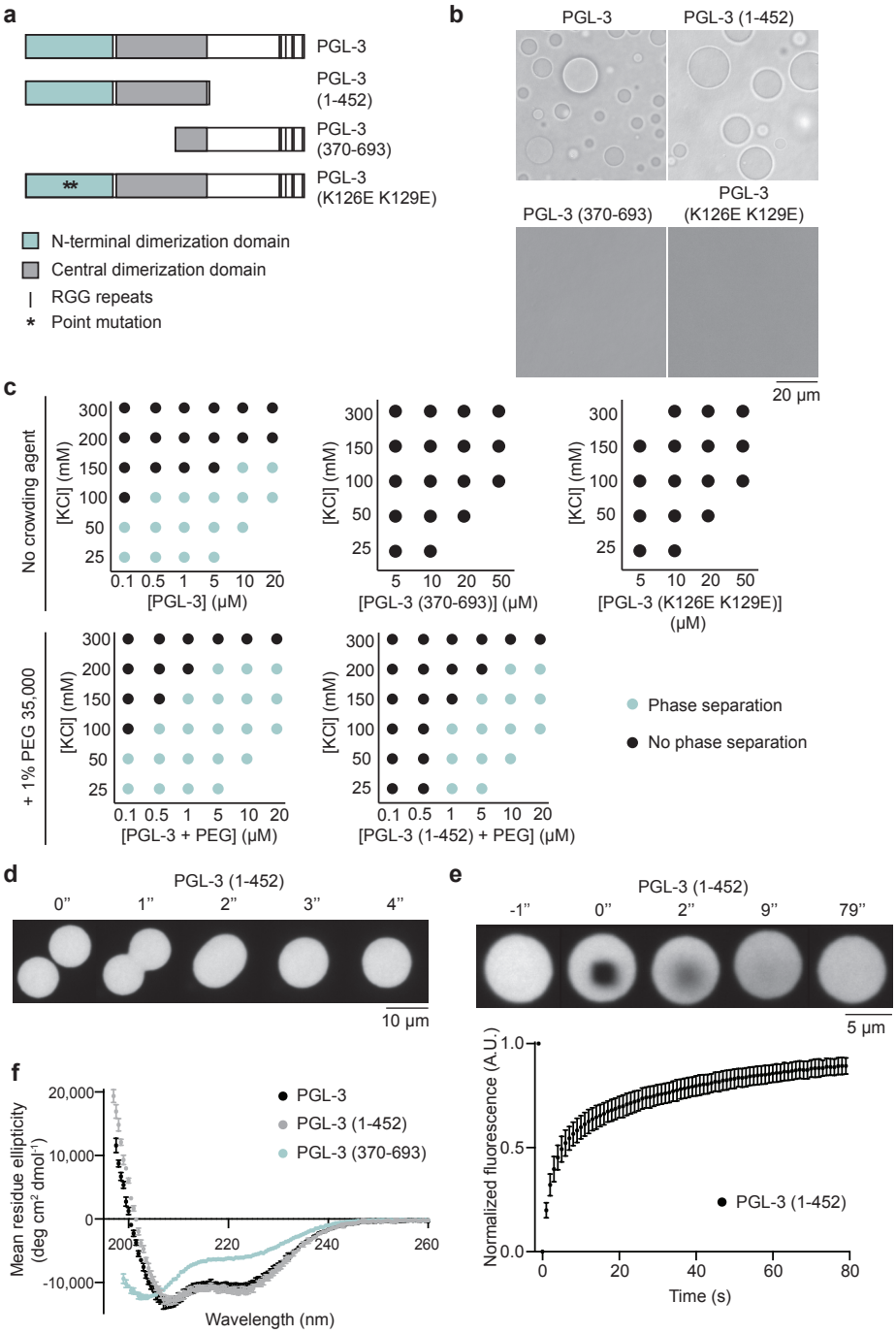

Fig. 1 α-helical N terminus drives phase separation of PGL-3.

a Cartoon representing PGL-3 and mutants. **b** Bright field micrographs of PGL-3 (23 µM), PGL-3 (1-452) (22 µM), PGL-3 (370-693) (67 µM) and PGL-3 (K126E K129E) (108 µM) in 25 mM HEPES pH 7.5, 100 mM KCl, 1 mM DTT in absence of crowding agents. Scale bar 20 µm. **c** Phase diagrams of PGL-3 and mutants at different protein and salt (KCl) concentrations. Blue circles represent conditions where phase separation was observed. Black circles represent conditions where phase separation was absent. Top row: Phase diagrams of PGL-3, PGL-3 (370-693), and PGL-3 (K126E K129E) in 25 mM HEPES pH 7.5, 1 mM DTT in absence of crowding agents. 5% of the pool of protein was tagged with mEGFP in each case. Bottom row: Phase diagrams of PGL-3, and PGL-3 (1-452) in 25 mM HEPES pH 7.5, 1 mM DTT, 1% PEG 35000. 5% of the pool of protein was tagged with mEGFP in each case. **d** Time-lapse fluorescence micrographs show fusion of two PGL-3 (1-452) condensates (5% tagged with mEGFP in 25 mM HEPES pH 7.5, 100 mM KCl, 1 mM DTT, 1% PEG 35000). Scale bar 10 µm. **e** Time-lapse fluorescence micrographs show fluorescence recovery after photobleaching in a condensate of PGL-3 (1-452) (5% tagged with mEGFP in 25 mM HEPES pH 7.5, 100 mM KCl, 1 mM DTT, 1% PEG 35000). Scale bar 5 µm. Shown below is a plot of average normalized fluorescence in bleached regions (1.5 µm x 1.5 µm) of the PGL-3 (1-452) condensates (n = 24) over time. Error bars represent 1 SD. **f** Plot of mean residue ellipticity of PGL-3 and mutants vs. wavelength assayed using circular dichroism (CD) spectroscopy. Black circles: PGL-3 (3 µM, 10 mM Potassium phosphate pH 7.5, 300 mM KCl, 1 mM TCEP), Grey circles: PGL-3 (1-452) (3 µM, 10 mM Potassium phosphate pH 7.5, 300 mM KCl, 1 mM TCEP), Blue circles: PGL-3 (370-693) (10 µM, 10 mM Potassium phosphate pH 7.5, 150 mM KCl, 1 mM TCEP). Error bars represent 1 SD among six CD scans.

182 terminal PGL-3 fragment (1-452) are liquid-like in nature. First, condensates are spherical in
183 shape (Fig. 1d, e, Supplementary Fig. 2d). Second, condensates fuse over time to generate
184 a larger condensate (Fig. 1d). Third, fluorescence recovery after photobleaching (FRAP)
185 experiments showed that PGL-3 (1-452) molecules intermix rapidly ($t_{1/2}$ = 4 s) within a
186 condensate (Fig. 1e). We conclude that phase separation of the protein PGL-3 is driven by
187 an α-helical region, while the disordered region may stabilize condensates by modulating
188 the driving forces for phase separation.
189
190 We next investigated how RNA impacts and alters the phase behaviour of PGL-3. It has
191 been previously shown that the PGL-3 protein cannot phase separate independently at
192 physiological concentration (Saha *et al*, 2016). At this concentration, sufficiently long mRNA
193 can trigger phase separation via binding to six arginine-glycine-glycine (RGG) repeats at
194 the C-terminal disordered region of PGL-3 (Saha *et al*, 2016). We therefore expected that
195 when the C-terminal disordered region was mixed with RNA, it would promote phase
196 separation. Unexpectedly, we found that in contrast to full-length PGL-3, mRNA does not
197 support phase separation of the C-terminal disordered region of PGL-3 (Fig. 2a, b). This
198 suggests that the N-terminal α-helical region is essential for phase separation. However, we
199 found that mRNA does not enhance phase separation of the N-terminal α-helical region of
200 PGL-3 either (Fig. 2a, b).
201
202 To investigate the underlying mechanism further, we began by testing if the N-terminal α-
203 helical region of PGL-3 can self-associate. Our analysis using size exclusion
204 chromatography followed by multi-angle light scattering (SEC-MALS) showed that this PGL-
205 3 fragment 1-452 forms a dimer (Supplementary Fig. 2f). Mutation of two residues (K126E
206 K129E) have been shown to interfere with interactions among the N-termini of PGL-3
207 molecules (Aoki *et al*, 2021). We mutated these two residues within the full-length PGL-3
208 protein (K126E K129E) (Fig. 1a) and found that this mutant PGL-3 (K126E K129E) protein
209 cannot phase separate even at high protein concentrations up to ~130 μM (Fig. 1b, c).
210 Addition of mRNA does not trigger phase separation of this protein at physiological
211 concentrations either (Fig. 2a, b). Taken together, our data is consistent with a model where
212 association among folded N-termini of PGL-3 molecules is essential for phase separation.

Fig. 2 Homotypic interaction among PGL-3 molecules is essential for mRNA-dependent phase separation.

a Fluorescence micrographs of PGL-3 and mutants (0.5 μM) in presence or absence of total mRNA (10 ng/μL). 5% of the pool of protein was tagged with mEGFP in each case. Buffer: 25 mM HEPES pH 7.5, 150 mM KCl, 1 mM DTT. 1% PEG 35,000 was added to PGL-3 (1-452). Scale bar 10 μm.
b Plot of the number of condensates with PGL-3 and mutants in presence or absence of total mRNA. For each condition, number of condensates was scored in nine different fluorescence micrographs (116 μm x 117 μm). Error bars represent 1 SD. t- test was performed to compare the number of condensates of each construct with or without the addition of total mRNA (p values: PGL-3: p = 1.04E-6; PGL-3 (1-452): p = 0.172; PGL-3 (370-693): p = 0.940; PGL-3 (K126E K129E): p = 0.828). The significance score was determined by the following criteria: ns: p > 0.05; ****: p ≤ 0.0001.
c Cartoon showing that at physiological concentrations, mRNA facilitates PGL-3 condensate formation. Association among folded N-termini of PGL-3 molecules is necessary for phase separation.

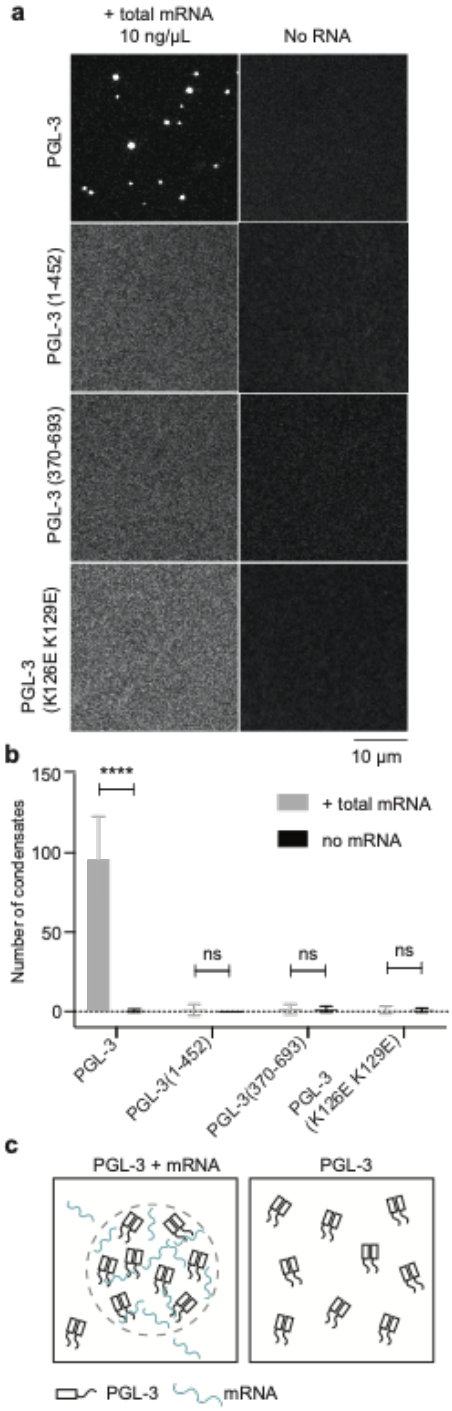

At physiological concentrations, mRNA facilitates this process by binding to the disordered C-terminus of PGL-3 (Fig. 2c).

α-helicity of PGL-3 correlates with dynamics in condensates in vitro.

P granules have a complex composition, containing mRNA and over forty proteins (Updike & Strome, 2010). It is unclear how dynamics within the P granule phase depends on interactions among those components. Two constitutive P granule proteins, PGL-1 and GLH-1, have been reported to exchange rapidly between the cytoplasm and liquid-like P granules in *C. elegans* gonads (FRAP half-time ($t_{1/2}$) = 7 – 28 s) (Brangwynne *et al*, 2009). Interestingly, in spite of their vastly reduced compositional complexity, we found that condensates generated in vitro with the PGL-3 protein alone show similar dynamics ($t_{1/2}$ = 7 s) (Supplementary Fig. 2c). To investigate the role of other P granule components on dynamics of PGL-3, we added mRNA and recombinantly purified PGL-1 and GLH-1 to condensates of PGL-3 in vitro at physiologically relevant proportions compared to PGL-3 (Saha *et al*, 2016). We found that PGL-1, GLH-1 and mRNA concentrate within

254 condensates of PGL-3 in vitro, but have a modest effect on the dynamics of PGL-3 ($t_{1/2}$ = 10
255 s) (Supplementary Fig. 2c). This suggests that the dynamics of full length PGL-3 are
256 intrinsic to the protein, and that the influence of complex composition on dynamics is
257 modest.
258
259 In order to address the interactions that drive dynamics within condensates, we began by
260 probing the dynamics of several PGL-3 constructs within phase-separated condensates in
261 vitro. The rate at which molecules of two PGL-3 constructs 1-452 and 1-577, that either lack
262 the disordered C-terminal region entirely or in part, rearrange within condensates are close
263 to full-length PGL-3 (Fig. 1e, Supplementary Fig. 2g, 3a, b). This suggests that interactions
264 involving the disordered C-terminal region of PGL-3 are not essential for the fast dynamics
265 within condensates. Therefore, we addressed the role of the N-terminal α-helical region (1-
266 452) in driving dynamics. In order to avoid engineering mutations that result in significant
267 misfolding of PGL-3 and concomitant loss of its ability to phase separate, we focused our
268 mutational analysis close to the junction of the folded N-terminus and the disordered C-
269 terminus of PGL-3. Surprisingly, we found that a full-length PGL-3 construct (Δ425-452) that
270 lacks only 27 residues phase separates into condensates that are non-dynamic (Fig. 3a, c).
271 Sequence analysis of the PGL-3 protein predicts that this region 425-452 spans two α-
272 helices (one complete helix and fraction of a second helix) (Supplementary Fig. 3d). We
273 generated a PGL-3 construct (hereafter called 'S1') (Fig. 3a) in which the sequence in the
274 region, 425-452, is shuffled while keeping the overall amino acid composition unchanged.
275 We found that S1 phase separates into condensates that are 20- fold less dynamic than
276 with wild-type PGL-3 (Fig. 3d, Supplementary Fig. 3c). Following assembly via phase
277 separation, the extremely slow dynamics in condensates of S1 does not change
278 significantly over 24 h (Supplementary Fig. 3f). Taken together, our data suggests that
279 interactions involving the N-terminal α-helical region of PGL-3 are required for fast
280 dynamics within condensates.
281
282 For more insights into the role of the N-terminal α-helical region in regulating dynamics
283 within condensates of PGL-3, we investigated the contribution of the region 425-452 further.
284 CD spectroscopy showed that α-helicity is reduced in the mutant S1 compared to wild-type
285 PGL-3 (Supplementary Fig. 3g). One possibility is that sequence-shuffling of residues 425-

452 changes the tertiary structure of PGL-3. Interestingly, we found that the mutant S1 can phase separate at concentrations lower than wild-type PGL-3 (Supplementary Fig. 3e). Further, mutation of two residues (K126E K129E), that interfere with interactions among the N-termini of wild-type PGL-3 molecules (Aoki *et al*, 2021), also inhibit phase separation of the S1 mutant even at high protein concentrations up to ~50 μM (Fig. 3a, Supplementary Fig. 3c, e). This suggests that, regardless of change in tertiary structure, interactions among the N-termini of S1 molecules are important for phase separation. In order to address the consequence of sequence-shuffling of residues 425-452 further, we compared the structural stability of S1 with wild-type PGL-3. We tested this through thermal unfolding which monitor α-helical content between 20 °C and 90 °C, using the CD signal at 222 nm as a measure of α-helical content. We found that wild-type PGL-3 unfolds in two phases as temperature is increased (T_m = 47 °C and 61 °C) (Fig. 3b). On the other hand, S1 also unfolds in two phases but sequence-shuffling results in lower thermostability (T_m = 41 °C and 61 °C) (Fig. 3b). Taken together, our observations on the phase separation behavior of the S1 mutant raises the possibility that loss of α-helicity of PGL-3 may correlate with slower dynamics in condensates.

In order to address if dynamics in condensates correlate with structural stability of PGL-3, we compared the dynamics of condensates formed via phase separation of folded and unfolded PGL-3 constructs. Heat-induced unfolding of both PGL-3 and S1 is irreversible (Supplementary Fig. 3h, i). These constructs do not recover lost α-helicity once the temperature is lowered to 21 °C following unfolding at higher temperatures. Therefore, we heated mEGFP-tagged PGL-3 and S1 proteins at different temperatures for 10 min followed by cooling to room temperature and triggering phase separation (by diluting salt (KCl) concentration to 150 mM). Wild-type PGL-3 does not lose α-helicity when heated to 43.5 °C (Supplementary Fig. 3h). We observed that PGL-3-mEGFP preheated at 43.5 °C generates condensates that are liquid-like (Fig. 3e). On the other hand, heating S1 to 43.5 °C results in partial unfolding (Supplementary Fig. 3i), and phase separation of this partially unfolded S1-mEGFP protein generates solid-like condensates with no observable FRAP recovery (Fig. 3f). Similarly, heating wild-type PGL-3 to a higher temperature (50 °C) results in partial unfolding (Supplementary Fig. 3h), and phase separation of this partially unfolded PGL-3-mEGFP protein generates solid-like condensates with no observable FRAP recovery (Fig.

3e). Taken together, our data suggests that reduced α-helicity of PGL-3 correlates with slower dynamics in condensates.

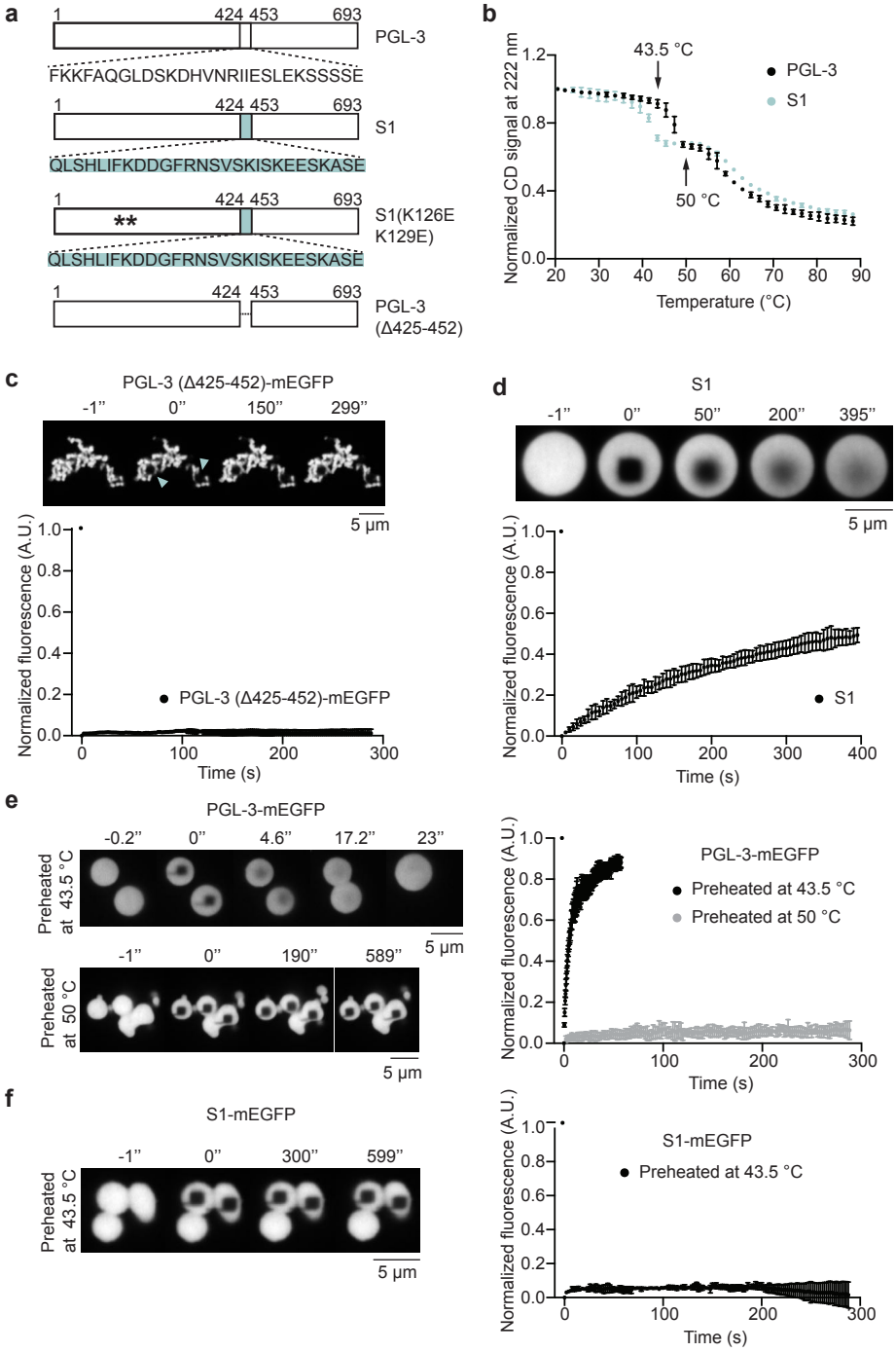

Fig. 3 α-helicity of PGL-3 correlates with dynamics in condensates.

a Cartoon representing PGL-3, S1, S1(K126E K129E) and PGL-3 (Δ425-452). Residues 425-452 of wild-type PGL-3 are shuffled in mutants S1 and S1(K126E K129E) . **b** Plot of normalized circular dichroism (CD) spectroscopy signal at 222 nm with PGL-3 (black circle) and S1 (blue circle) vs. temperature, assayed at 5 µM protein concentration in 25 mM HEPES pH 7.5, 1 M KCl, 1 mM DTT. Error bars represent 1 SD among three independent measurements. Arrows highlight 43.5 °C and 50 °C – temperatures where partial unfolding of PGL-3 begins and ends respectively. **c-d** Time-lapse fluorescence micrographs show fluorescence recovery after photobleaching in condensates of **c** PGL-3 (Δ425-452)-mEGFP or **d** S1 (5% of the pool of protein was tagged with mEGFP). Arrowheads show photobleached area in condensates of PGL-3 (Δ425-452)-mEGFP. Scale bars 5 µm. Shown below the time-lapse micrographs are plots of average normalized fluorescence over time **c** in bleached regions (1.4 µm x 1.4 µm) of PGL-3 (Δ425-452)-mEGFP condensates (n = 8) or **d** in bleached regions (1.5 µm x 1.5 µm) of S1 (5% tagged with mEGFP) condensates (n = 18). Error bars represent 1 SD. **e** Time-lapse fluorescence micrographs show fluorescence recovery after photobleaching at room temperature in condensates of PGL-3-mEGFP (preheated at 43.5 °C or 50 °C). Scale bar 5 µm. Shown next to the micrographs is a plot of average normalized fluorescence over time in bleached regions (1.4 µm x 1.4 µm) within the condensates of PGL-3-mEGFP preheated at 43.5 °C (black circles, n =8) or 50 °C (grey circles, n = 8). Error bars represent 1 SD. **f** Time-lapse fluorescence micrographs show fluorescence recovery after photobleaching at room temperature in condensates of S1-mEGFP (preheated at 43.5 °C). Scale bar 5 µm. Shown next to the micrographs is a plot of average normalized fluorescence over time in bleached regions (1.4 µm x 1.4 µm) within the condensates of S1-mEGFP preheated at 43.5 °C (n =8). Error bars represent 1 SD.

372
373 **P granule components buffer against reduced dynamics in condensates.**
374 We wanted to see if similar changes in dynamics are seen in P granules in *C. elegans*
375 worms. To address this, we injected mEGFP-tagged wild-type PGL-3 or S1 proteins into
376 gonads of adult *C. elegans* and investigated their dynamics. Both PGL-3-mEGFP and S1-
377 mEGFP target to perinuclear P granules (Fig. 4a). Fluorescence recovery after
378 photobleaching experiments showed that S1 exchanges between P granules and
379 cytoplasm at rates similar to wild-type PGL-3 (Fig. 4b, Supplementary Fig 4a). Similarly,
380 when partially unfolded PGL-3-mEGFP (preheated at 50 °C) is injected into gonads of adult
381 *C. elegans*, this protein concentrates in perinuclear P granules (Fig. 4a) and exchanges
382 between P granules and cytoplasm at rates similar to wild-type PGL-3 (Fig. 4b,
383 Supplementary Fig 4a). Experiments with microinjected mutant PGL-3 proteins most likely
384 assay the effect of the P granule phase on high non-physiological dose of partially
385 denatured PGL-3 proteins. To test the effect on a physiologically expressed mutant PGL-3
386 protein, we used CRISPR/Cas9 technology to generate a transgenic strain that expresses
387 the construct PGL-3 (Δ425-452)-mEGFP from the native *pgl-3* locus. We found that PGL-3
388 (Δ425-452)-mEGFP concentrates in perinuclear puncta (Fig. 4c) and shows dynamics
389 similar to wild-type PGL-3-mEGFP (Fig. 4e, Supplementary Fig. 4b, Supplementary Movie
390 1 and 2). Further, we found that fecundity of the strain expressing PGL-3 (Δ425-452)-
391 mEGFP is similar to the strain expressing PGL-3-mEGFP (Fig. 4d). This suggests that the
392 P granule phase can prevent slowdown of dynamics and associated loss-of-function
393 resulting from the expression of the aggregation-prone PGL-3 (Δ425-452)-mEGFP
394 construct. Taken together, our results suggest that the multicomponent P granule phase
395 can prevent slowdown of dynamics associated with reduced α-helicity of PGL-3.
396
397 To reconstitute the multicomponent nature of the P granule, we purified and added back
398 other P granule proteins to the PGL-3 phase formed in vitro. Interestingly, addition of
399 merely a few P granule components (mRNA and recombinantly purified PGL-1 and GLH-1)
400 to condensates of S1 in vitro enhances the dynamics of S1 almost 20-fold to match the
401 dynamics observed in condensates of wild-type PGL-3 (Fig. 4f, Supplementary Fig. 4c-e,
402 5f). Further, we found that dynamics within condensates of S1 can be significantly
403 enhanced simply by adding wild-type PGL-3 protein (Supplementary Fig. 5a). For better

404 insight into how the PGL-3 protein supports fast dynamics of S1, we added three different
405 PGL-3 constructs (the N-terminal α-helical fragment 1-452, the C-terminal fragment 370-
406 693, and the phase separation-incompetent mutant PGL-3 (K126E K129E)) at different
407 concentrations to condensates of S1. We found that all three PGL-3 constructs concentrate
408 within condensates of S1 to different degrees (Supplementary Figure 5c) and enhance the
409 dynamics of S1 (Supplementary Fig. 5a). Further, addition of the phase separation-
410 incompetent mutant S1 (K126E K129E) to condensates of S1 also enhanced the dynamics
411 of S1 within condensates (Supplementary Fig. 5a and 5c). Taken together, our data
412 suggests that enhanced S1 dynamics in condensates can be supported by a wide variety of
413 interactions involving other P granule components (PGL-1, GLH-1, mRNA) or different parts
414 of the PGL-3 protein.
415

Fig. 4 P granule components promote fast dynamics of PGL-3 constructs with reduced α-helicity.

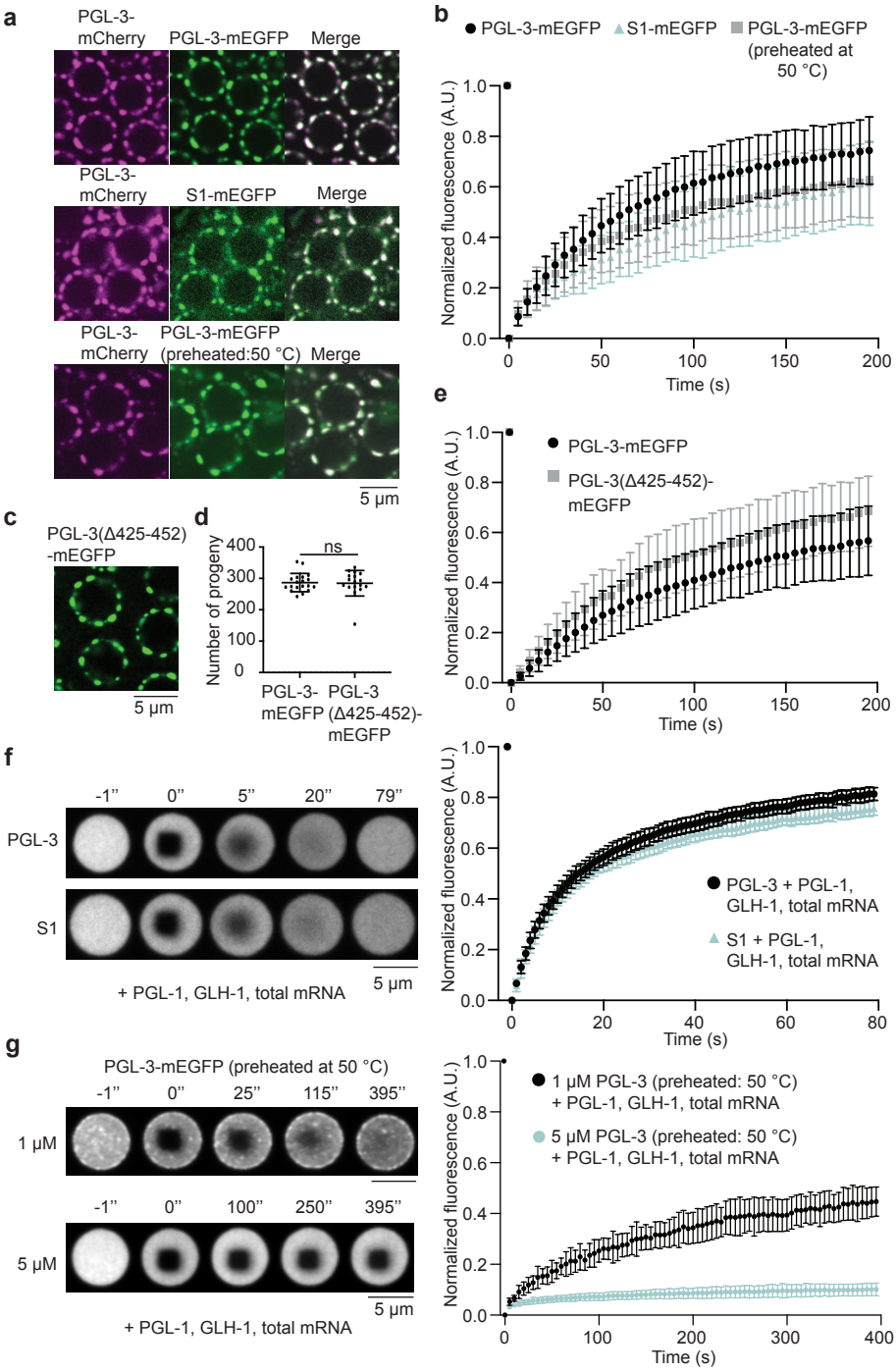

a Fluorescence micrographs of gonads (pachytene region) in *C. elegans* expressing PGL-3-mCherry (shown in magenta) injected with recombinantly-purified PGL-3-mEGFP, S1-mEGFP, or PGL-3-mEGFP preheated at 50 °C (shown in green). A single confocal section is shown. Scale bar 5 µm.
b Plot showing average normalized fluorescence signal over time in bleached peri-nuclear regions (1.5 µm x 1.5 µm) in wild-type *C. elegans* gonads (pachytene region) injected with recombinantly purified PGL-3-mEGFP (black circles, n = 46), S1-mEGFP (blue triangles, n = 36), or PGL-3-mEGFP preheated at 50 °C (grey circles, n = 37). Error bars represent 1 SD. For each condition, data from 2 different animals injected with a recombinantly purified protein were analyzed. Statistical analysis of the estimated half times of fluorescence recovery is shown in Supplementary Fig. 4a.
c Fluorescence micrograph of gonad (pachytene region) in *C. elegans* expressing PGL-3 (Δ425-452)-mEGFP (shown in green). A single confocal section is shown. Scale bar 5 µm.
d Plot showing total number of progeny of worms expressing PGL-3-mEGFP (n=19) or PGL-3 (Δ425-452)-mEGFP (n=17) at 20 °C. Each black circle represents the number of progenies from a single worm. The mean and 1 SD are also indicated. For statistical analysis, T test was performed (p = 0.858). "ns" indicates no significant difference (p > 0.05) between the number of progenies of the two genotype.
e Plot showing average normalized fluorescence signal over time in bleached peri-nuclear regions in *C. elegans* gonads (pachytene region) expressing either PGL-3-mEGFP (black circles, n = 43) or PGL-3 (Δ425-452)-mEGFP (grey squares, n = 32). Error bars represent 1 SD. For each condition, data from 6 different animals were analyzed. Statistical analysis of the estimated half times of fluorescence recovery is shown in Supplementary Fig. 4b.
f Time-lapse fluorescence micrographs show fluorescence recovery after photobleaching over time in condensates of PGL-3 (5 µM) or S1 (5 µM) (5% of the pool of protein was tagged with mEGFP) in presence of PGL-1 (6.7 µM), GLH-1 (1 µM), and total mRNA (14 ng/µL). Scale bar 5 µm. Shown next to the micrographs is a plot of average normalized fluorescence over time in bleached regions (1.5 µm x 1.5 µm) within the condensates of PGL-3 (black circles, n = 20) or

472 S1 (blue triangles, n = 21) in presence of PGL-1, GLH-1 and total mRNA. Error bars represent 1 SD. Statistical analysis of
473 the estimated half times of fluorescence recovery is shown in Supplementary Fig. 4c.
474 **g** Time-lapse fluorescence micrographs show fluorescence recovery after photobleaching over time in condensates of
475 PGL-3-mEGFP preheated at 50 °C in presence of PGL-1 (6.7 μM), GLH-1 (1 μM), and total mRNA (14 ng/μL).
476 Concentration of PGL-3-mEGFP used: 1 μM or 5 μM. Scale bar 5 μm. Shown next to the micrographs is a plot of average
477 normalized fluorescence over time in bleached regions (1.5 μm x 1.5 μm) within the condensates of PGL-3-mEGFP
478 preheated at 50 °C. Black circles, 1 μM PGL-3-mEGFP (n = 14) and blue circles, 5 μM PGL-3-mEGFP (n = 15). Error bars
479 represent 1 SD.
480
481 We next wondered if addition of other P granule components is able to support or rescue a
482 dynamic state of partially unfolded PGL-3 within condensates. In contrast to S1, which
483 generates condensates that are liquid-like, partially unfolded PGL-3-mEGFP (preheated at
484 50 °C) phase separates into non-dynamic solid-like condensates in vitro (Fig. 3e). We
485 tested the ability of different components to rescue dynamics of partially unfolded PGL-3-
486 mEGFP. When P granule components (mRNA and recombinantly purified PGL-1 and GLH-
487 1) are added to partially unfolded PGL-3-mEGFP at concentrations similar to those used
488 with S1 (5 μM), the PGL-3 protein phase separates predominantly into non-dynamic
489 condensates (Fig. 4g, Supplementary Fig. 4f, g). However, when a lower concentration of
490 the partially unfolded PGL-3 protein is used (1 μM), addition of these P granule components
491 supports its phase separation into liquid-like condensates (Fig. 4g). These results revealed
492 a concentration-dependence to the extent with which unfolded PGL-3 impacts condensate
493 dynamics.
494
495 We wondered if, similar to partially unfolded PGL-3-mEGFP, the dynamics of S1 also
496 depends on its concentration. In the assays in which S1 is mixed with different additional
497 components, 5% of the total pool of S1 is tagged with mEGFP. This allowed us to measure
498 the dynamics of S1 within condensates using FRAP. Following photobleaching,
499 fluorescence recovered in bleached region within condensates in two phases – a fast phase
500 driven predominantly by internal rearrangement of molecules within the condensate, and a
501 slower phase driven by the exchange with the pool of unbleached molecules outside the
502 condensate (Supplementary Fig. 6a-f). We focused on the fast phase of recovery and used
503 single-exponential fits to estimate half-time of internal rearrangement of S1 molecules
504 within condensates of different composition. On addition of other P granule components
505 (PGL-1, GLH-1, mRNA) to different concentrations of S1, we found that the half-time of
506 FRAP recovery of S1 within condensates remains relatively unchanged in spite of almost 5-
507 fold change in mEGFP-fluorescence signal per unit area within the condensates (Fig. 5a).

508 Assuming that mEGFP-fluorescence reports on the concentration of S1, this observation
509 suggests that P granule components can buffer the dynamics of S1 close to rates observed
510 in condensates of wild-type PGL-3 alone (Fig. 5a, d). However, the dynamics of S1 slows
511 down above a threshold concentration (9 μM in Fig. 5a), suggesting that P granule
512 components can buffer the dynamics of S1 only within a range of concentrations in
513 condensates. We wondered if the observed dynamics buffering effect within condensates of
514 S1 is limited to the specific set of additives PGL-1, GLH-1 and mRNA. We assayed this by
515 adding to condensates of S1 the construct PGL-3 (K126E K129E). The mutations K126E
516 K129E are expected to interfere with interactions among N-termini of S1 and PGL-3 (K126E
517 K129E) molecules (Aoki *et al*, 2021). We found that addition of this phase separation-
518 incompetent mutant PGL-3 (K126E K129E) can also buffer dynamics within a 2- fold range
519 of S1 concentration within condensates (Fig. 5b). However, the buffering is different
520 compared to when PGL-1, GLH-1 and mRNA are added. Specifically, the range of
521 concentrations of S1 in condensates where dynamics is buffered and the associated half-
522 time of FRAP recovery depend on the additives. We used condensates of similar size for
523 our analysis (average ± 1 SD of diameter of condensates are 6.4 ± 1.7 μm (Fig. 5a) and 5.9
524 ± 0.4 μm (Fig. 5b)). Therefore, dynamics buffering here is likely to represent similar
525 diffusion rates of S1 within condensates.
526
527 For more insights into how addition of different components rescues slowdown of S1
528 dynamics within condensates, we added wild-type PGL-3, or different PGL-3 or S1
529 constructs to condensates of S1. These additives titrated the concentration of S1 within
530 condensates (tracked by S1-mEGFP fluorescence signal per unit area) over a range
531 spanning concentration observed with condensates of S1 alone and those in presence of
532 other P granule components (PGL-1, GLH-1, mRNA). Here, we found that the half-time of
533 FRAP recovery of S1 correlates with mEGFP-fluorescence signal per unit area within the
534 condensates (Fig. 5c). This suggests that, regardless of the condensate composition, fast
535 dynamics generally correlate with smaller concentrations of S1. In control assays, we found
536 that the dynamics of the wild-type PGL-3 protein does not correlate significantly with either
537 concentration of PGL-3 or the composition of the condensate (Fig. 5d, Supplementary Fig.
538 5b, d).
539

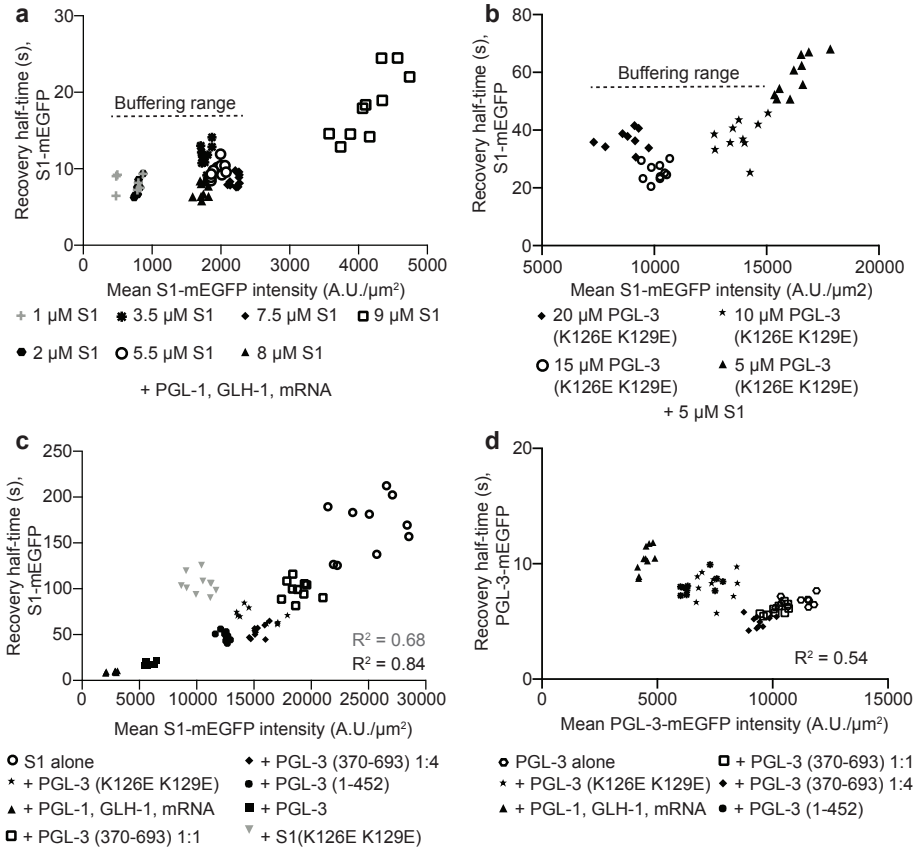

Fig. 5 Dynamics of S1 in condensates of different composition.

Analysis of fluorescence recovery after photobleaching within 1.5 μm x 1.5 μm regions in condensates of different composition. Half-time of fluorescence recovery after photobleaching ($t_{1/2}$) in each case was estimated by fitting the data to a single-exponential curve (see methods section for details). **a** Plot of $t_{1/2}$ vs. mean S1-mEGFP fluorescence intensity per unit area (before photobleaching) within condensates. Each point on the plots represents data from a single photobleached region within a condensate of defined composition which includes 5 μM PGL-1, 0.75 μM GLH-1, 11 ng/ μM mRNA and different S1 concentrations indicated as follows. Grey plus: 1 μM S1, solid hexagon: 2 μM S1, asterisk 3.5 μM S1, open circle: 5.5 μM S1, solid diamond: 7.5 μM S1, solid triangle: 8 μM S1, open square: 9 μM S1. Ten points are plotted for each composition (seven for 1 μM S1) and buffering range indicates a range of S1 concentrations where $t_{1/2}$ does not differ significantly between different conditions.
b Plot of t1/2 vs. mean S1-mEGFP fluorescence intensity per unit area (before photobleaching) within condensates. Each point on the plots represents data from a single photobleached region within a condensate of defined composition which includes 5 μM S1 and different concentrations of PGL-3 (K126E K129E) indicated as follows. Solid diamond: 20 μM PGL-3 (K126E K129E), open circle: 15 μM PGL-3 (K126E K129E), asterisk 10 μM PGL-3 (K126E K129E), solid triangle: 5 μM PGL-3 (K126E K129E), Ten points are plotted for each composition (nine for 20 μM PGL-3 (K126E K129E)) and buffering range indicates a range of S1 concentrations where t1/2 does not differ significantly between different conditions.
c Plot of $t_{1/2}$ vs. mean S1-mEGFP fluorescence intensity per unit area (before photobleaching) within condensates. Each point on the plots represents data from a single photobleached region within a condensate of defined composition as follows. Open circle: S1 alone (10 μM, 5% mEGFP-tagged), solid diamond: S1 (5 μM, 5% mEGFP-tagged) + PGL-3 (370-693) (20 μM), solid asterisk: S1 (5 μM, 5% mEGFP-tagged) + PGL-3 (K126E K129E) (5 μM), solid circle: S1 (5 μM, 5% mEGFP-tagged) + PGL-3 (1-452) (5 μM), solid triangle: S1 (5 μM, 5% mEGFP-tagged) + PGL-1 (6.7 μM) + GLH-1 (1 μM) + total mRNA (14 ng/μL), solid square: S1 (5 μM, 5% mEGFP-tagged) + PGL-3 (5 μM), open square: S1 (5 μM, 5% mEGFP-tagged) + PGL-3 (370-693) (5 μM), grey inverse triangle: S1 (5 μM, 5% mEGFP-tagged) + S1(K126E K129E) (5 μM). Ten points are plotted for each composition. All or part of the data were fit using linear regression (R^2 = 0.68, fit of all data; R^2 = 0.84, fit of data on all compositions excluding S1+ S1(K126E K129E)). Data points for S1+ S1(K126E K129E) are highlighted since S1(K126E K129E) is the only construct added to S1 which contains the shuffled 425-452 region.
d Plot of $t_{1/2}$ vs. mean PGL-3-mEGFP fluorescence intensity per unit area (before photobleaching) within condensates. Each point on the plots represents data from a single photobleached region (1.5 μm x 1.5 μm) within a condensate of defined composition as follows. Open hexagon: PGL-3 alone (10 μM, 5% mEGFP-tagged), open square: PGL-3 (5 μM, 5% mEGFP-tagged) + PGL-3 (370-693) (5 μM), solid asterisk: PGL-3 (5 μM, 5% mEGFP-tagged) + PGL-3 (K126E K129E) (5 μM), solid diamond: PGL-3 (5 μM, 5% mEGFP-tagged) + PGL-3 (370-693) (20 μM), solid triangle: PGL-3 (5 μM, 5% mEGFP-tagged) + PGL-1 (6.7 μM) + GLH-1 (1 μM) + total mRNA (14 ng/μL), solid circle: PGL-3 (5 μM, 5% mEGFP-tagged) + PGL-3 (1-452) (5 μM). Ten points are plotted for each composition and R^2 value for a linear regression fit among all compositions is indicated.

596

597 **Discussion**

598 To maintain homeostasis, cellular liquid-like compartments must be functionally robust
599 against small changes in composition or denaturation of one or more of its components.
600 The mechanisms that provide such robustness remain unclear. A recent study proposed
601 that liquid-liquid phase separation may reduce variation in concentration of components
602 within condensates (Klosin *et al*, 2020). It remains unclear if LLPS can similarly buffer
603 diffusion rate of components within condensates. Recent studies with simple two-
604 component LLPS systems showed that the behavior of one component can influence the
605 dynamics of another within condensates (Boeynaems *et al*, 2019; Rhine *et al*, 2020; Zhang
606 *et al*, 2015; Alshareedah *et al*, 2021). While components are expected to influence the
607 dynamics of each other within multi-component condensates, it is unclear *a priori* how
608 dynamics of biomolecular condensates with complex composition adapt to
609 misfolding/denaturation of one or more component proteins. Here, we show that the liquid-
610 like P granule phase can rescue slow-down of diffusion rate associated with denaturation of
611 a component protein. Such dynamics-buffering may contribute to functional robustness of
612 cellular liquid-like compartments.

613

614 In order to understand how composition supports dynamics-buffering in biomolecular
615 condensates, we began by addressing why denaturation of the PGL-3 protein leads to
616 slower dynamics in condensates. One possibility is that the conformational changes of
617 PGL-3 associated with reduced α-helicity facilitate stronger inter-molecular interactions. For
618 instance, loss of α-helicity could increase the valence of “stickers” leading to additional
619 physical crosslinks among PGL-3 molecules (Choi *et al*, 2020). Stronger inter-molecular
620 interactions could inhibit rapid rearrangement of interacting partners within condensates,
621 resulting in slower dynamics. Alternatively, interactions involving unfolded or partially
622 unfolded PGL-3 molecules could generate inter-polypeptide chain entanglements within
623 condensates resulting in slower dynamics. With diffusion of PGL-3 molecules within
624 condensates, more entanglements could develop over time resulting in further decrease in
625 dynamics. Few observations suggest that slower dynamics within PGL-3 condensates
626 result predominantly from stronger inter-molecular interactions in contrast to inter-chain
627 entanglements. First, dynamics of the mutant S1 protein within condensates does not

628 change significantly over 24 h. Second, the mutations K126E K129E that interfere with
629 interactions among PGL-3 or S1 molecules (Aoki *et al*, 2021) help enhance dynamics of S1
630 molecules within condensates. For instance, when added to condensates of S1, both S1
631 (K126E K129E) and PGL-3 (K126E K129E) help enhance the dynamics of S1 within
632 condensates. Addition of S1 (K126E K129E) reduces concentration of S1 within
633 condensates more than addition of PGL-3 (K126E K129E). However, dynamics of S1 within
634 condensates is faster in spite of higher concentration with PGL-3 (K126E K129E). Taken
635 together, these observations support the model that slow dynamics of S1 within
636 condensates depend on interactions among S1 molecules and suggest that interaction
637 among S1 molecules is stronger than that between wild-type PGL-3 molecules. Stronger
638 interaction among S1 molecules is further supported by the observation that S1 molecules
639 can phase separate at lower concentrations compared to wild-type PGL-3 molecules
640 (Supplementary Fig. 3e).
641
642 Our data is consistent with the model that other regions of S1 molecules cooperate with
643 residues 425-452 (shuffled) to generate stronger inter-molecular interactions. For instance,
644 addition of the mutant S1 (K126E K129E) enhances dynamics of S1 within condensates in
645 contrast to maintaining the slower dynamics observed within condensates of S1 alone. This
646 suggests that the interactions disrupted by the mutations K126E and K129E also contribute
647 to slow S1 dynamics. One possibility is that interactions involving the residues K126 and
648 K129 favor S1 conformations that enhance 425-452 (shuffled)-dependent interactions.
649 Indeed, the mutations K126E K129E have been reported to interfere with interactions
650 among N-termini of PGL-3 molecules (Aoki *et al*, 2021). While two self-association domains
651 within the α-helical N-terminus of PGL-3 have been mapped (Aoki *et al*, 2021, 2016),
652 structural insights into those associations are limited. However, PGL-3 shares significant
653 sequence similarity with another protein PGL-1. Crystal structures are available for
654 fragments of the PGL-1 protein that show the two self-association domains at the N-
655 terminus are predominantly α-helical and globular in nature (Aoki *et al*, 2016, 2021).
656 Therefore, one possibility is that shuffling the sequence 425-452 of PGL-3 or heat-induced
657 unfolding of PGL-3 exposes hydrophobic residues that become available to participate in
658 inter-molecular interactions. This effect may be enhanced within phase separated
659 condensates if the local solvent environment favors more extended conformations of the

660 PGL-3 protein, allowing more inter-molecular interactions compared to within the
661 surrounding dilute phase. Indeed, recent studies reported that a 129- residue long
662 intrinsically disordered fragment of the human Tau protein or the prion-like low complexity
663 domain of hnRNPA1 preferentially sample more extended conformations within phase-
664 separated condensates compared to the surrounding dilute phase (Majumdar *et al*, 2019;
665 Bremer *et al*, 2021). Taken together, our data suggests that strength of inter-molecular
666 interactions regulate dynamics within condensates of PGL-3.
667
668 It is generally thought that chaperone proteins or RNA helicases counteract slow-down
669 of dynamics that may result from denaturation of components or inter-
670 polypeptide/RNA chain entanglements in biomolecular condensates. For instance, the
671 ATPase-dependent activity of chaperones is required to dissolve aberrant stress granules
672 that result from aggregation of misfolding-prone proteins (Ganassi *et al*, 2016; Mateju *et al*,
673 2017). In contrast, we discovered that weak interactions among two or more components
674 can buffer against large change of dynamics within the P granule phase. This effect is
675 distinct from active processes that depend on ATP hydrolysis. Specifically, we show that
676 presence of just three P granule components (PGL-1, GLH-1 and mRNA) is sufficient to
677 support a dynamic state of partially unfolded PGL-3-mEGFP within phase-separated
678 condensates. In absence of the P granule components, partially unfolded PGL-3-mEGFP
679 phase separates into non-dynamic condensates. We found that the ability of P granule
680 components to support a dynamic state of partially unfolded PGL-3-mEGFP depends on
681 the relative concentrations and hence stoichiometries of PGL-3 and the P granule
682 components. This suggests that P granule components support dynamics by participating in
683 inter-molecular interactions with PGL-3-mEGFP molecules. Similarly, different PGL-3
684 constructs – PGL-3 (K126E K129E), PGL-3 (1-452) and PGL-3 (370-693) enhanced
685 dynamics of S1 molecules within condensates to different degrees. This may correlate with
686 the varying ability of these constructs to interact with S1 molecules. We considered the
687 specificity of interactions that support fast dynamics within phase separated condensates.
688 Our data showing that different additives (P granule components, or wild-type PGL-3, or
689 PGL-3 constructs that differ in terms of their ability to fold or self-associate) can all rescue
690 slowdown of dynamics of the mutant S1 protein within condensates suggest that fast
691 dynamics can be supported by competing interactions among two or more components

692 (Fig. 6). Future investigations will reveal the individual contribution of different P granule
693 proteins to dynamics buffering. Similar to our data with P granules, interactions among
694 components could be a potential mechanism of storage of misfolding-prone proteins in non-
695 aggregated state within the liquid-like nucleolus under stress in vivo (Frottin *et al*, 2019).
696 We speculate that these interactions that support fast dynamics are weak in nature and
697 allow fast dissociation rates. Taken together, our study supports the possibility that weak
698 interactions among two or more components prevent aggregation or large change of
699 dynamics within cellular liquid-like compartments.
700
701 An interesting aspect of the dynamics buffering effect is that the dynamics of S1 remain
702 relatively unchanged regardless of the change of S1 concentration within condensates. The
703 buffering capacity depends on the additives i.e. the range of intra-condensate S1
704 concentrations where dynamics is buffered varies with additives. Once the buffering
705 capacity is exhausted i.e. beyond a threshold intra-condensate S1 concentration, dynamics
706 of S1 molecules slow down at higher S1 concentrations. More work is required to
707 understand the underlying mechanism. One possibility is that dynamics is buffered when
708 the relative concentration of S1 molecules and additives within condensates remain
709 unchanged. The “buffered” dynamics of S1 molecules within condensates also vary with
710 additives. We found that dynamics of S1 molecules is faster in presence of P granule
711 components (PGL-1, GLH-1 and mRNA) compared to that with the mutant PGL-3 (K126E
712 K129E). Future work will reveal if the buffered dynamics depend on the number of
713 interacting species within condensates (e.g. four when PGL-1, GLH-1 and mRNA is added
714 to condensates of S1; two when PGL-3 (K126E K129E) is added to S1 condensates) in
715 addition to the strength/nature of inter-molecular interactions.
716

Fig. 6 Weak interactions among two or more components promote fast dynamics in condensates.

Cartoon shows how dynamics in condensates change with composition. Each condensate contains one or more of three different macromolecules (depicted as thread, square and hexagon) at different concentrations. Homotypic interactions among threads are strong. Other homotypic and heterotypic interactions are weak. Dynamics generally correlate inversely with concentration of strong interactors in condensates. However, within a range of low concentrations of strong interactors, heterotypic interactions can buffer, at least in part, against significant change of dynamics.

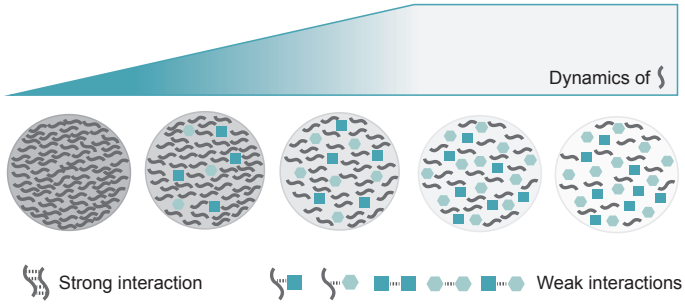

Many cellular non-membrane-bound compartments have been characterized to contain two or more phases with distinct biophysical properties (Banani *et al*, 2017; Feric *et al*, 2016; Jain *et al*, 2016; Lyon *et al*, 2021; Wang *et al*, 2014). Further, within the same liquid-like phase, diffusion rates of two different components may differ from each other (Boeynaems *et al*, 2019; Mathieu *et al*, 2020; Zhang *et al*, 2015). In P granules of *C. elegans* early embryos, a gel-like phase of MEG proteins is known to associate with the liquid-like phase of PGL proteins (Wang *et al*, 2014; Smith *et al*, 2016; Putnam *et al*, 2019). The gel-like phase of MEG proteins is absent from P granules of adult *C. elegans* gonads. Two recent studies suggest that association of the gel-like MEG phase changes the surface tension of the liquid-like PGL phase without changing its viscosity or the diffusion rates of PGL proteins (Folkmann *et al*, 2021; Putnam *et al*, 2019). Taken together, one possibility is that the dynamics-buffering mechanism that we identified here adds stability to the steady-state dynamics of liquid-like phases.

An important part of our study is to show that interactions among the α-helical N-terminal domain of PGL-3 molecules can drive phase separation. Although the unstructured C-terminus is dispensable for phase separation of PGL-3, it fine-tunes the process. First, full-length PGL-3 can phase separate at concentrations lower than the α-helical N-terminus 1-452 alone (Fig. 1c), suggesting that interactions involving the C-terminus enhance the propensity of phase separation. Second, heterotypic interactions among the unstructured C-terminus of PGL-3 molecules and mRNA facilitate phase separation of PGL-3 (Saha *et al*, 2016). Our data is consistent with other studies which found that interactions involving both folded domains and intrinsically disordered regions of proteins drive liquid-liquid phase

separation to assemble many cellular non-membrane-bound compartments (Guillén-Boixet *et al*, 2020; Mittag & Parker, 2018; Yang *et al*, 2020).

The concept of robustness is widely understood to be essential for the ability of genetic circuits to function under a wide variety of perturbations (Félix & Barkoulas, 2015). We propose that one route to achieving robustness is through condensates that contribute to spatial and temporal regulation over biochemical reactions. The compositional heterogeneity-dependent dynamics-buffering mechanism that we identified here could add robustness to biochemical reactions within condensates against the deleterious consequences of stresses, short-term effects of chemical modifications, intrinsic mutational changes, and the problems that arise from accumulating high local concentrations of sticky molecules. The ability to buffer against these changes to dynamics not only provides robustness, but these networks of interactions could also provide a source of variation that enable responsiveness when conditions change.

770 **Materials and Methods**

771 **Protein expression and purification**

772 All PGL-3, GLH-1 and PGL-1 constructs were purified recombinantly from insect cells using
773 a baculovirus infection system. Insect cells were harvested ~72 hours after viral infection
774 and lysed. Constructs were purified from lysates using a combination of Ni-NTA affinity,
775 anion exchange and/or size exclusion chromatography as described below.

776

777 *PGL-3, PGL-1, PGL-3 (370-693) and PGL-3 (K126E K129E):* The protocol for purification of
778 PGL-3-6xHis-mEGFP has been described earlier (Saha et al., 2016). PGL-3-6xHis-RFP,
779 PGL-1-6xHis-mEGFP, PGL-3 (370-693)-6xHis-mEGFP and PGL-3 (K126E K129E)-6xHis-
780 mEGFP were purified using the same protocol.

781

782 *PGL-3 (1-452):* Insect cells expressing PGL-3 (1-452)-6xHis-mEGFP were resuspended in
783 lysis buffer (25 mM HEPES pH 7.5, 300 mM KCl, 0.3 M L-Arginine, 10 mM Imidazole, 1 mM
784 DTT added with protease inhibitor cocktail Complete EDTA-free (Roche) and lysed using
785 sonicator. The lysates were centrifuged at 21,000 x g in a JS-13.1 rotor (Beckman-Coulter),
786 and Ni-NTA Agarose resin (Macherey-Nagel) was mixed with the supernatant to capture
787 PGL-3 protein molecules. The resin was then washed with 25 mM HEPES pH 7.5, 0.3 M
788 KCl, 20 mM Imidazole. Finally, the PGL-3 molecules were eluted into 25 mM HEPES pH
789 7.5, 300 mM KCl, 250 mM Imidazole.

790 In preparation for anion-exchange chromatography, the eluate from Ni-NTA column
791 was diluted 1:5 in 25 mM Tris pH 8.0, 1 mM DTT and 5 ml of Q Sepharose resin (GE
792 Healthcare) was mixed to capture PGL-3 protein molecules. After incubation for ~1 h, the
793 resin was washed with 25 mM Tris pH 8.0, 1 mM DTT buffers containing 350 mM, 500 mM
794 and 1 M KCl. The eluates in 25 mM Tris pH 8.0, 1 mM DTT buffers containing 500 mM KCl
795 and 1 M KCl were pooled together and further purified using size exclusion chromatography
796 with a TSKgel 5000PW column (Tosoh Bioscience) in 25 mM HEPES pH 7.5, 1 M KCl, 1
797 mM DTT.

798

799 *PGL-3 (1-577):* Insect cells expressing PGL-3 (1-577)-6xHis-mEGFP were resuspended in
800 lysis buffer (25 mM HEPES pH 7.25, 300 mM KCl, 10 mM Imidazole, 1 mM DTT added with
801 protease Inhibitor cocktail set III (Calbiochem) and lysed via passage through Avestin

802 Emulsiflex C5. The lysates were centrifuged at 20000 rpm in a Ti45 rotor (Beckman-
803 Coulter), and Ni-NTA Agarose resin (Qiagen) was mixed with the supernatant to capture
804 PGL-3 protein molecules. The resin was then washed with 25 mM HEPES pH 7.25, 300
805 mM KCl, 20 mM Imidazole, 1 mM DTT. Finally, the PGL-3 molecules were eluted into 25
806 mM HEPES pH 7.25, 300 mM KCl, 250 mM Imidazole.
807 In preparation for anion-exchange chromatography, the eluate from Ni-NTA column
808 was diluted 1:6 in 25 mM Tris pH 8.0, 1 mM DTT and 5-10 ml of Q Sepharose resin (GE
809 Healthcare) was mixed to capture PGL-3 protein molecules. After incubation for ~1 h, the
810 resin was washed with 25 mM Tris pH 8.0, 1 mM DTT buffers containing 100 mM, 200 mM,
811 350 mM, 500 mM and 1 M KCl. The PGL-3 molecules eluted into the 25 mM Tris pH 8.0, 1
812 mM DTT buffers containing 500 mM KCl and 1 M KCl.
813 The eluates were further purified using size exclusion chromatography with HiLoad
814 16/60 Superdex 200 column (GE Healthcare) in 25 mM HEPES pH 7.5, 0.3 M KCl, 1 mM
815 DTT. The fractions containing pure PGL-3 (1-577)-6xHis-mEGFP from both runs were
816 pooled together.
817
818 *S1 and S1(K126E K129E):* Insect cells expressing PGL-3 (S1)-6xHis-mEGFP or PGL-3
819 (S1(K126E K129E))-6xHis-mEGFP were resuspended in lysis buffer (25 mM HEPES pH
820 7.5, 300 mM KCl, 300 mM L-Arginine, 10 mM Imidazole, 1 mM DTT added with protease
821 inhibitor cocktail Complete EDTA-free (Roche) and lysed using sonicator. The lysates were
822 centrifuged at 21,000 x g in a JS-13.1 rotor (Beckman-Coulter), and Ni-NTA Agarose resin
823 (Macherey-Nagel) was mixed with the supernatant to capture PGL-3 protein molecules. The
824 resin was then washed with 25 mM HEPES pH 7.5, 1 M KCl, 20 mM Imidazole. Finally, the
825 PGL-3 molecules were eluted into 25 mM HEPES pH 7.5, 1 M KCl, 250 mM Imidazole.
826 Next, 500 units of Benzonase nuclease and 1 mM each of DTT and $MgCl_2$ were added to
827 the eluate and dialyzed overnight into 25 mM HEPES pH 7.5, 1 M KCl, 1 mM DTT, 1 mM
828 $MgCl_2$.
829 In preparation for anion-exchange chromatography, the dialysate was diluted 1:13 in
830 25 mM Tris pH 8.0, 1 mM DTT and 5-10 ml of Q Sepharose resin (GE Healthcare) was
831 mixed to capture PGL-3 protein molecules. After incubation for ~1 h, the resin was washed
832 with 25 mM Tris pH 8.0, 350 mM KCl, 1 mM DTT and finally the PGL-3 molecules were
833 eluted into 25 mM Tris pH 8.0, 1 M KCl, 1 mM DTT.

834 The eluates were further purified using size exclusion chromatography with a TSKgel
835 5000PW column (Tosoh Bioscience) in 25 mM HEPES pH 7.5, 1 M KCl, 1 mM DTT.
836
837 *PGL-3 (Δ425-452):* Insect cells expressing PGL-3 (Δ425-452)-6xHis-mEGFP were
838 resuspended in lysis buffer (25 mM HEPES pH 7.25, 300 mM KCl, 300 mM L-Arginine, 10
839 mM Imidazole, 1 mM DTT, 10 mM $MgCl_2$ added with protease Inhibitor cocktail set III
840 (Calbiochem) and Benzonase nuclease) and lysed via passage through Avestin Emulsiflex
841 C5. The lysates were centrifuged at 20000 rpm in a Ti45 rotor (Beckman-Coulter), and Ni-
842 NTA Agarose resin (Qiagen) was mixed with the supernatant to capture PGL-3 protein
843 molecules. The resin was then washed with 25 mM HEPES pH 7.25, 1 M KCl, 40 mM
844 Imidazole, 1 mM DTT. Finally, the PGL-3 molecules were eluted into 25 mM HEPES pH
845 7.25, 1 M KCl, 250 mM Imidazole, 1 mM DTT. Next, ~250 units of Benzonase nuclease and
846 10 mM $MgCl_2$ were added to the eluate and dialyzed overnight into 25 mM HEPES pH 7.25,
847 1 M KCl, 1 mM DTT, 10 mM $MgCl_2$.
848 In preparation for anion-exchange chromatography, the dialysate was diluted 1:12 in
849 25 mM Tris pH 8.0, 1 mM DTT and 5-10 ml of Q Sepharose resin (GE Healthcare) was
850 mixed to capture PGL-3 protein molecules. After incubation for ~1 h, the resin was washed
851 with 25 mM Tris pH 8.0, 320 mM KCl, 1 mM DTT and the PGL-3 (Δ425-452) molecules
852 were eluted into 25 mM Tris pH 8.0, 500 mM KCl, 1 mM DTT. Finally, the eluate containing
853 purified PGL-3 (Δ425-452)-6xHis-mEGFP was dialyzed into 25 mM HEPES pH 7.5, 1 M
854 KCl, 1 mM DTT.
855
856 *GLH-1*: Insect cells expressing GLH-1-6xHis-mEGFP were resuspended in lysis buffer (25
857 mM HEPES pH 7.5, 300 mM KCl, 10 mM Imidazole, 1 mM DTT added with protease
858 inhibitor cocktail Complete EDTA-free (Roche) and lysed using sonicator. The lysates were
859 centrifuged at 21,000 x g in a JS-13.1 rotor (Beckman-Coulter), and Ni-NTA Agarose resin
860 (Macherey-Nagel) was mixed with the supernatant to capture PGL-3 protein molecules. The
861 resin was then washed with 25 mM HEPES pH 7.5, 300 mM KCl, 20 mM Imidazole. Finally,
862 the GLH-1 molecules were eluted into 25 mM HEPES pH 7.5, 300 mM KCl, 250 mM
863 Imidazole.
864 In preparation for anion-exchange chromatography, the eluate was diluted 1:6 in 25
865 mM Tris pH 8.0, 1 mM DTT and 4 ml of Q Sepharose resin (GE Healthcare) was mixed to

866 capture GLH-1 protein molecules. After incubation for ~30 min, the resin was washed with
867 25 mM Tris pH 8.0, 1 mM DTT buffers containing 200 mM, 250 mM, 300 mM, 350 mM, 400
868 mM, 500 mM and 1 M KCl. The fractions with 250 to 350 mM KCl were pooled.
869 Pooled fractions were further purified using size exclusion chromatography with a
870 HiLoad 16/60 Superdex 200 column (GE Healthcare) in 25 mM HEPES pH 7.5, 300 mM
871 KCl, 1 mM DTT.
872
873 *Untagged PGL-3, S1, PGL-3 (1-452), PGL-3 (370-693), PGL-3 (K126E K129E), S1 (K126E*
874 *K129E), PGL-1 and GLH-1* were purified by cleaving off 6xHis and mEGFP tags from the
875 C-terminus of the recombinant proteins using 6xHis-tagged TEV protease, followed by
876 incubation with Ni-NTA Agarose resin to remove 6xHis-tagged mEGFP and TEV protease.
877
878 **Size exclusion chromatography and multi-angle light scattering**
879 Molecular weight analysis of PGL-3 (1-452) was carried out using an OMNISEC multi-
880 detector instrument from Malvern Panalytical. All measurements were performed in 25 mM
881 HEPES, 300 mM KCl, 1 mM TCEP at 25°C. Prior to measurement, samples were
882 centrifuged at 10 000 g for 10 min. 90 µl of sample at 0.5 mg/ml was injected onto a
883 Superose 6 10/300 column (Cytiva). The eluate from the column was fed into a refractive
884 index detector followed by a right-angle light scattering detector (640 nm). Data were
885 analysed using the OMNISEC software (v11.10) using a refractive index increment (dn/dc)
886 of 0.185 ml/g. Bovine serum albumin (PierceTM) was used to calibrate the detectors.
887 Samples were measured in duplicate.
888
889 **Labeling of proteins with fluorescent dye**
890 In order to generate fluorescently labeled S1, PGL-1 and GLH-1, the proteins were first
891 dialyzed into buffer containing 1 mM TCEP and then incubated with AlexaFluor 594 C5-
892 maleimide (Invitrogen) in 25 mM HEPES pH 7.5, 300 mM KCl (1 M KCl for S1), 1 mM
893 TCEP for 2 h at room temperature. To remove unbound dye, repeated buffer exchange was
894 performed with 25 mM HEPES pH 7.5, 300 mM KCl (1 M KCl for S1), 1 mM TCEP until no
895 fluorescence was detected in the flow through.
896
897

898 **Preparation of mRNA used in experiments**
899 In order to track the localization of mRNA in our assays, fluorescently labeled mRNA was
900 generated using in vitro transcription. Coding sequence of the act-4 gene from *C. elegans*
901 was cloned to be transcribed from a T7 promoter. To generate in vitro transcribed act-4
902 mRNA, T7 RNA polymerase (New England BioLabs) was used and ribonucleotide solution
903 mix was doped with 30% Aminoallyl-UTP-Cy5 (Jena Bioscience). The reaction was
904 incubated for 1 h at 37 °C, then treated with DNase II and mRNA was finally purified using
905 RNeasy Mini Kit (Qiagen). For all the other experiments, total mouse liver mRNA (Takara)
906 was used.
907
908 **Imaging and fluorescence recovery after photobleaching (FRAP) experiments**
909 Phase separation properties of PGL-3 constructs under various conditions were imaged
910 within chambers created by attaching cover glass to glass slide with imaging spacer
911 between them (Grace Bio-Labs SecureSeal, Sigma Aldrich). 4 µL of solution was placed at
912 the center of the imaging chamber, such that the spacer had no contact with the solution.
913 PGL-3 (1-452) (Fig. 1b) was imaged directly on the cover glass (without glass slide), as
914 condensates of PGL-3 (1-452) were not stable when imaged within the glass chamber.
915 Addition of 1% crowding agent PEG-35000 stabilized condensates of this N-terminal
916 fragment of PGL-3 allowing imaging over time (Fig. 1c-e, 2a, 2b, Supplementary Fig. 2d).
917 The surfaces of glass slide and cover glass were passivated through PEG-silanization as
918 described earlier (Alberti et al., 2018).
919
920 The images were acquired with an inverted microscope (Olympus IX83) equipped with a
921 spinning-disk scan head (4,000 rpm, Yokogawa CSU-W1), a sCMOS camera (pixel size
922 11um, Prime 95B Teledyne Photometrics), and a 100x/1.4 oil-immersion objective
923 (Olympus UPLSAPO). For imaging and FRAP experiments, we used Coherent OBIS lasers
924 of wavelengths 405nm (FRAP), 488 nm, 561 nm, and 640 nm. Single confocal plane was
925 imaged over time for all FRAP experiments.
926
927 Phase separation properties of the PGL-3 constructs PGL-3 (1-577), PGL-3 (Δ425-452) and
928 FRAP experiments of preheated PGL-3-mEGFP and S1-mEGFP were imaged within flow
929 chambers created by attaching cover glass to glass slide with two double-sided tapes (~60

930 μm thick) positioned parallel to each other. The surface of the cover glass was passivated
931 through PEG-silanization or coating with lipids as described earlier (Alberti et al., 2018). An
932 inverted spinning-disk confocal imaging system was used, fitted with diode-pumped solid-
933 state LASERs (wavelength 488 nm and 561 nm), Olympus UplanSApochromat 100x 1.4
934 NA oil-immersion objective, Yokogawa CSU-X1 (5000 rpm) spinning-disk scan head, and
935 Andor iXon DU-897 BV back illuminated EMCCD camera.
936
937 **Image analysis**
938 All image analysis was conducted using the Fiji image-processing package (http://fiji.sc/Fiji).
939 Images used for analysis of FRAP experiments were corrected for camera noise and
940 uneven illumination error. Intensities of the bleached areas were corrected for bleaching
941 and normalized to prebleached image. FRAP data was fitted to single exponential function
942 using Matlab (Supplementary figure 5e). All fits had R^2 value of 0.92 or higher.
943
944 FRAP data for the construct S1(K126E K129E) was acquired with the same spinning-disk
945 confocal imaging system as all other constructs, but a different FRAP filter was used. To
946 account for any difference in signal intensity resulting from the use of a different FRAP filter,
947 we compared the fluorescence intensities of S1-mEGFP, PGL-3-mEGFP and a uniformly
948 green fluorescent slide (Chroma Autofluorescent Plastic Slides) in images acquired using
949 the two different FRAP filters. This analysis using three different samples all gave similar
950 values of correction factor around 2.6. We used this correction factor to normalize the
951 intensities of S1(K126E K129E) and plotted the results in Fig. 5c.
952
953 **Phase separation assays**
954 For phase separation assays, different recombinantly-purified PGL-3 constructs were used,
955 and phase separation was triggered by diluting salt (KCl) concentration to either 150 mM or
956 100 mM in 25 mM HEPES, pH 7.5, 1 mM DTT. Following phase separation, condensates of
957 PGL-3 (1-452) dissolved rapidly when incubated within glass-based imaging chambers.
958 Addition of 1% crowding agent PEG-35000 stabilized condensates of this N-terminal
959 fragment of PGL-3 allowing imaging over time.
960

961 In some cases, PGL-3 constructs were preheated at higher temperatures (43.5 °C or 50 °C)
962 for 10 min, followed by incubation at room temperature for 10 mins and phase separation
963 via dilution of salt concentration. Incubation at higher temperatures was carried out in a
964 temperature-controlled water bath or PCR thermocycler. Heating untagged wild-type PGL-3
965 and the mutant S1 protein at 50 °C or 43.5 °C respectively resulted in aggregation. In
966 contrast, presence of mEGFP tag reduced the extent of heat-induced aggregation to a large
967 extent. Therefore, we used mEGFP-tagged PGL-3 constructs in these assays. Following
968 incubation at 43.5 °C or 50 °C, we centrifuged the samples (5 min at 20,000 g) to separate
969 the aggregates from the pool of soluble protein in the supernatant. To account for loss of
970 protein via aggregation, we remeasured the concentration of protein in the supernatant and
971 used this pool of mEGFP-tagged PGL-3 constructs for our assays.
972
973 At physiological concentrations (approx. 1 μM), the PGL-3 protein is unable to phase
974 separate into condensates in vitro (Saha *et al*, 2016). At these concentrations, mRNA
975 promotes phase separation of PGL-3 (Saha *et al*, 2016). To assay for mRNA-dependence
976 of condensate assembly, it is therefore essential to use physiological concentrations of wild-
977 type or mutant PGL-3 proteins (Figure 2). However, these condensates are generally too
978 small to assay rate of internal rearrangement of PGL-3 molecules within condensates using
979 fluorescence recovery after photobleaching experiments. Therefore, to generate large
980 condensates for measuring internal rearrangement of wild-type or mutant PGL-3 molecules,
981 we primarily used higher concentrations of these proteins in vitro (binding to RNA is not
982 essential for phase separation at these concentrations). However, to mimic the in vivo P
983 granule phase as closely as possible, we generally added constituent proteins in proportion
984 to their in vivo abundance (Saha *et al*, 2016) as described below.
985
986 In assays investigating phase separation of two or more components (i.e. PGL-3, S1,
987 different PGL-3 constructs, PGL-1, GLH-1 or mRNA), the components were mixed with
988 each other before phase separation was triggered by diluting the salt (KCl) to final
989 concentration of 100 mM in 25 mM HEPES pH 7.5, 1 mM DTT. In experiments where we
990 studied the correlation between concentration of S1 or PGL-3 in condensates and their half-
991 time of FRAP recovery: 1) all tested mixtures contained the same concentration of S1 (5
992 μM) or PGL-3 (5 μM) and 5% of the protein pool of S1 or PGL-3 was mEGFP-tagged; 2)

993 Image acquisition settings were the same for all the experimental groups: 50 ms exposure;
994 488-laser power set to 100%; bleaching power set to 100%.
995
996 We used fluorescently labeled PGL-3 constructs, PGL-1, GLH-1 or act-4 mRNA to check if
997 they colocalize with S1 or PGL-3 in condensates. All components were mixed with each
998 other before phase separation was triggered by diluting the salt (KCl) to final concentration
999 of 100 mM in 25 mM HEPES pH 7.5, 1 mM DTT. In these experiments, 5% of the pool of
1000 PGL-3 or S1 proteins was fluorescently labeled. 100% of the other components in the mix
1001 were labeled with a fluorescent probe. Colocalization of different PGL-3 constructs with
1002 wild-type PGL-3 or S1 was tested by adding the different proteins in equal amounts (final
1003 concentration of each component was 5 μM). In experiments where colocalization of
1004 different P granule components with PGL-3 or S1 was assayed, concentration (or
1005 concentration ratio) of the different components were the same as in FRAP experiments
1006 (6.7 μM PGL-1, and 14 ng/ μL mRNA with 5 μM S1 or 5 μM PGL-3; 1 μM GLH-1 with 5 μM
1007 PGL-3; 2 μM GLH-1 with 10 μM S1).
1008
1009 ***C. elegans* strains, maintenance and transgenic strain construction**
1010 *C. elegans* strains were maintained on plates containing nematode growth media seeded
1011 with OP50 bacteria using standard methods (Brenner, 1974). The strains TH561, TH623
1012 and SSA130 were generated using CRISPR/Cas9-based technology (Table 1). Strains
1013 were verified by sequencing of the modified locus.
1014
1015 **Table 1. *C. elegans* strains used in this study.**

***C. elegans* strain number**	**Genotype**	**Guide RNA sequence**	**Source**
SSA27	N2 (wild-type)	-	CGC
TH561	*pgl-3(dd29[pgl-3::mEGFP]) V*	5'GAAGGCTTAGGAACCTCCAC3'	This study
TH623	*pgl-3(knu99[pgl-3::mCherry]) V*	5'GGATTCTTTGGTGGATCCCG3' 5'TTCTTTGGTGGATCCCGTGG3'	This study (generated by InVivo Biosystems)
SSA130	*pgl3(sds130[pgl-3(Δ425-452)::mEGFP]) V*	5'GATCACAGAGTTCTACGGAT3'	This study

1016

1017 **Fecundity assay**

1018 We assayed fecundity of the worms TH561 (*pgl-3::mEGFP*) and SS130 (*pgl-3(Δ425-*
1019 *452)::mEGFP*). These animals were grown and maintained at 20 °C throughout the
1020 experiment. L4 worms were singled for each strain. Each of these worms was transferred to
1021 a fresh plate every 24 h for five days. On the fourth day after transfer to a fresh plate, the
1022 number of progenies from each animal was scored. The total number of progenies for each
1023 worm was calculated and shown in Fig. 4d.

1024

1025 **Microinjection of recombinant proteins into *C. elegans* gonads**

1026 Recombinant PGL-3 constructs were microinjected into gonads of young adult *C. elegans*
1027 to study 1) their colocalization with P granules, and 2) the effect of the P granule phase on
1028 their dynamics. To study colocalization, mEGFP-tagged PGL-3 constructs were injected
1029 into gonads of worms expressing PGL-3-mCherry (strain TH623) from the native locus (to
1030 track P granules). Concentrations of injected proteins: PGL-3-mEGFP (10 μM), S1-mEGFP
1031 (6 μM) and PGL-3-mEGFP preheated at 50 °C (30 μM). To minimize the effect of
1032 fluorescent tag on dynamics, FRAP experiments were conducted on N2 worms
1033 microinjected with mEGFP-tagged PGL-3 constructs. Concentration of injected proteins:
1034 PGL-3-mEGFP (20 μM), S1-mEGFP (25 μM) and PGL-3-mEGFP preheated at 50 °C (30
1035 μM). Worms were immobilized using 2 mM levamisole and imaged immediately following
1036 injections.

1037

1038 **Circular Dichroism (CD) spectroscopy**

1039 CD spectroscopy of PGL-3 constructs was carried out in a quartz cuvette (0.5 mm
1040 pathlength) using Chirascan Plus spectrometer (Applied Photophysics) equipped with TC1
1041 temperature controller (Quantum Northwest). To measure the change in α- helical content
1042 of PGL-3 at different temperatures (data presented in Fig. 3b), the temperature of the
1043 cuvette was varied from 20 °C to 90 °C in 2 °C steps. At each temperature, the system was
1044 allowed to equilibrate for 180 s before measurement of CD signal between 200 and 260
1045 nm. To test if unfolding of PGL-3 constructs at higher temperature is reversible once the
1046 temperature is lowered (data presented in Supplementary Fig. 3h and i), CD signal was
1047 measured initially at 21 °C, followed by measurements at a higher temperature (43.5 °C or

1048 50 °C) and once again after the temperature was lowered back to 21 °C. At each
1049 temperature, the system was allowed to equilibrate for 15 min before measurement of CD
1050 signal between 200 and 260 nm.
1051
1052 **Statistical analysis**
1053 Two-tailed t test was performed for comparing two groups of data (number of condensates
1054 with or without addition of mRNA in Fig 2b; number of progeny in Fig 4d; estimated half
1055 time of recovery of fluorescence signal for bleached P granules in TH561 (*pgl-3::mEGFP*)
1056 and SSA130 (*pgl-3(Δ425-452)::mEGFP*) in Supplementary Fig. 4b; estimated half time of
1057 recovery of fluorescence signal for bleached condensates of S1 and PGL-3 with addition of
1058 PGL-1, GLH-1 and mRNA in Supplementary Fig. 4c). One way ANOVA was performed for
1059 comparing three groups of data (estimated half time of recovery of fluorescence signal for
1060 bleached P granules for injected proteins: PGL-3, PGL-3 preheated at 50 °C and S1 in
1061 Supplementary Fig. 4a). p values are indicated in the figure legends. Statistical tests were
1062 performed using GraphPad Prism version 8.4.3 (GraphPad Software, San Diego, California
1063 USA). To estimate the half time of recovery for above mentioned statistical analysis, the
1064 data points for normalized fluorescence signal for individual P granule/condensate were fit
1065 using R (RStudio Version 1.2.1335) to the following equation: $F_t = (F_0 + F_\infty*(t/t_{1/2}))/(1 + t/t_{1/2})$
1066 where F_t is fluorescence signal at time t, F_0 is fluorescence signal immediately after
1067 photobleaching (minimal fluorescence signal), F_∞ is maximal recovered fluorescence signal
1068 and $t_{1/2}$ is half time of fluorescence recovery (Yguerabide *et al*, 1982). Only high-confidence
1069 fits [i.e., goodness of fit ($p < 1E-11$)] were used for statistical tests.
1070
1071 **Acknowledgments**
1072 We thank A.A. Hyman, R.V. Pappu, A. Goloborodko for feedback on the manuscript and
1073 helpful discussions. We thank A.A. Hyman and C. Hoege for the *C. elegans* strains TH623
1074 and TH561. We thank Jana Sipkova, Anoop Kumar Yadav and Felicitas Arlt for help with
1075 image analysis and technical support. S.S. initiated this study as a postdoctoral fellow in the
1076 lab of A.A. Hyman. We thank the services and facilities at Vienna BioCenter for support -
1077 IMBA BioOptics Facility for support with imaging and image analysis; IMBA Molecular
1078 Biology Service for providing reagents for cloning and recombinant protein purification, and
1079 sequencing of constructs; VBCF Protein Technologies for help with recombinant protein

expression and performing SEC-MALS experiment; IMBA Protein Chemistry Facility for verification of recombinant proteins using mass spectrometry; VBCF Computational Biology Training (A. Aszódi) for help with generating scripts for curve fitting. N2 strain was provided by the CGC, which is funded by NIH Office of Research Infrastructure Programs (P40 OD010440). S.J., J.B., P.C., B.R.P., and S.S. are funded by the Austrian Academy of Sciences. A.S.H. is scientific advisor at Dewpoint Therapeutics.

Author contribution: Conceptualization, S.J. and S.S.; Methodology, S.J., A.S.H. and S.S.; Investigation, S.J., J.B., P.C., B.R.P., M.R., C.H., S.S.; Writing – Original Draft, S.J. and S.S.; Writing – Review & Editing, S.J., A.S.H., and S.S.; Funding Acquisition, S.S.; Resources, A.S.H. and S.S.; Supervision, S.S.

References

Alshareedah I, Thurston GM & Banerjee PR (2021) Quantifying viscosity and surface tension of multicomponent protein-nucleic acid condensates. *Biophysical Journal* 120: 1161–1169

Aoki ST, Kershner AM, Bingman CA, Wickens M & Kimble J (2016) PGL germ granule assembly protein is a base-specific, single-stranded RNase. *Proceedings of the National Academy of Sciences of the United States of America*

Aoki ST, Lynch TR, Crittenden SL, Bingman CA, Wickens M & Kimble J (2021) C. elegans germ granules require both assembly and localized regulators for mRNA repression. *Nat Commun* 12: 996

Banani SF, Lee HO, Hyman AA & Rosen MK (2017) Biomolecular condensates: organizers of cellular biochemistry. *Nature reviews Molecular cell biology* 18: 285–298

Banani SF, Rice AM, Peeples WB, Lin Y, Jain S, Parker R & Rosen MK (2016) Compositional Control of Phase-Separated Cellular Bodies. *Cell* 166: 651–663

Boeynaems S, Holehouse AS, Weinhardt V, Kovacs D, Van Lindt J, Larabell C, Van Den Bosch L, Das R, Tompa PS, Pappu RV, *et al* (2019) Spontaneous driving forces give rise to protein-RNA condensates with coexisting phases and complex material properties. *Proceedings of the National Academy of Sciences of the United States of America* 116: 7889–7898

Brangwynne CP, Eckmann CR, Courson DS, Rybarska A, Hoege C, Gharakhani J, Jülicher F & Hyman AA (2009) Germline P granules are liquid droplets that localize by controlled dissolution/condensation. *Science* 324: 1729–1732

Bremer A, Farag M, Borcherds WM, Peran I, Martin EW, Pappu RV & Mittag T (2021) Deciphering how naturally occurring sequence features impact the phase behaviors of disordered prion-like domains Biophysics

Brenner S (1974) The genetics of Caenorhabditis elegans. *Genetics* 77: 71–94

Choi J-M, Holehouse AS & Pappu RV (2020) Physical Principles Underlying the Complex Biology of Intracellular Phase Transitions. *Annual review of biophysics* 49: 107–133

Cipriani PG, Bay O, Zinno J, Gutwein M, Gan HH, Mayya VK, Chung G, Chen J-X, Fahs H, Guan Y, *et al* (2021) Novel LOTUS-domain proteins are organizational hubs that recruit C. elegans Vasa to germ granules. *Elife* 10: e60833

Elbaum-Garfinkle S, Kim Y, Szczepaniak K, Chen CC-H, Eckmann CR, Myong S & Brangwynne CP (2015) The disordered P granule protein LAF-1 drives phase separation into droplets with tunable viscosity and dynamics. *Proc Natl Acad Sci U S A* 112: 7189–7194

Félix M-A & Barkoulas M (2015) Pervasive robustness in biological systems. *Nature Reviews Genetics* 16: 483–496

1129 Feric M, Vaidya N, Harmon TS, Mitrea DM, Zhu L, Richardson TM, Kriwacki RW, Pappu RV
1130 & Brangwynne CP (2016) Coexisting Liquid Phases Underlie Nucleolar
1131 Subcompartments. *Cell*: 1–13

1132 Folkmann AW, Putnam A, Lee CF & Seydoux G (2021) Regulation of biomolecular
1133 condensates by interfacial protein clusters. *Science* 373: 1218–1224

1134 Frottin F, Schueder F, Tiwary S, Gupta R, Körner R, Schlichthaerle T, Cox J, Jungmann R,
1135 Hartl FU & Hipp MS (2019) The nucleolus functions as a phase-separated protein
1136 quality control compartment. *Science* 365: 342–347

1137 Ganassi M, Mateju D, Bigi I, Mediani L, Poser I, Lee HO, Seguin SJ, Morelli FF, Vinet J,
1138 Leo G, *et al* (2016) A Surveillance Function of the HSPB8-BAG3-HSP70 Chaperone
1139 Complex Ensures Stress Granule Integrity and Dynamism. *Molecular cell* 63: 796–
1140 810

1141 Guillén-Boixet J, Kopach A, Holehouse AS, Wittmann S, Jahnel M, Schlüßler R, Kim K,
1142 Trussina IREA, Wang J, Mateju D, *et al* (2020) RNA-Induced Conformational
1143 Switching and Clustering of G3BP Drive Stress Granule Assembly by Condensation.
1144 *Cell* 181: 346-361.e17

1145 Hanazawa M, Yonetani M & Sugimoto A (2011) PGL proteins self associate and bind RNPs
1146 to mediate germ granule assembly in C. elegans. *The Journal of Cell Biology* 192:
1147 929–937

1148 Jain S, Wheeler JR, Walters RW, Agrawal A, Barsic A & Parker R (2016) ATPase-
1149 Modulated Stress Granules Contain a Diverse Proteome and Substructure. *Cell* 164:
1150 487–498

1151 Jawerth L, Fischer-Friedrich E, Saha S, Wang J, Franzmann T, Zhang X, Sachweh J, Ruer
1152 M, Ijavi M, Saha S, *et al* (2020) Protein condensates as aging Maxwell fluids.
1153 *Science* 370: 1317–1323

1154 Kawasaki I, Amiri A, Fan Y, Meyer N, Dunkelbarger S, Motohashi T, Karashima T,
1155 Bossinger O & Strome S (2004) The PGL family proteins associate with germ
1156 granules and function redundantly in Caenorhabditis elegans germline development.
1157 *Genetics* 167: 645–661

1158 Kawasaki I, Shim YH, Kirchner J, Kaminker J, Wood WB & Strome S (1998) PGL-1, a
1159 predicted RNA-binding component of germ granules, is essential for fertility in C.
1160 elegans. *Cell* 94: 635–645

1161 Klosin A, Oltsch F, Harmon T, Honigmann A, Jülicher F, Hyman AA & Zechner C (2020)
1162 Phase separation provides a mechanism to reduce noise in cells. *Science* 367: 464–
1163 468

1164 Lyon AS, Peeples WB & Rosen MK (2021) A framework for understanding the functions of
1165 biomolecular condensates across scales. *Nat Rev Mol Cell Biol* 22: 215–235

1166 Majumdar A, Dogra P, Maity S & Mukhopadhyay S (2019) Liquid-Liquid Phase Separation
1167 Is Driven by Large-Scale Conformational Unwinding and Fluctuations of Intrinsically
1168 Disordered Protein Molecules. *The Journal of Physical Chemistry Letters* 10: 3929–
1169 3936

1170 Mateju D, Franzmann TM, Patel A, Kopach A, Boczek EE, Maharana S, Lee HO, Carra S,
1171 Hyman AA & Alberti S (2017) An aberrant phase transition of stress granules
1172 triggered by misfolded protein and prevented by chaperone function. *The EMBO*
1173 *journal* 36: 1669–1687

1174 Mathieu C, Pappu RV & Taylor JP (2020) Beyond aggregation: Pathological phase
1175 transitions in neurodegenerative disease. *Science* 370: 56–60

1176 Mittag T & Parker R (2018) Multiple Modes of Protein-Protein Interactions Promote RNP
1177 Granule Assembly. *Journal of molecular biology* 430: 4636–4649

1178 Phillips CM & Updike DL (2022) Germ granules and gene regulation in the Caenorhabditis
1179 elegans germline. *Genetics* 220: iyab195

1180 Price IF, Hertz HL, Pastore B, Wagner J & Tang W (2021) Proximity labeling identifies
1181 LOTUS domain proteins that promote the formation of perinuclear germ granules in
1182 C. elegans. *Elife* 10: e72276

1183 Putnam A, Cassani M, Smith J & Seydoux G (2019) A gel phase promotes condensation of
1184 liquid P granules in Caenorhabditis elegans embryos. *Nat Struct Mol Biol* 26: 220–
1185 226

1186 Rhine K, Makurath MA, Liu J, Skanchy S, Lopez C, Catalan KF, Ma Y, Ha T, Chemla YR &
1187 Myong S (2020) ALS/FTLD-Linked Mutations in FUS Glycine Residues Cause
1188 Accelerated Gelation and Reduced Interactions with Wild-Type FUS. *Molecular cell*

1189 Riback JA, Zhu L, Ferrolino MC, Tolbert M, Mitrea DM, Sanders DW, Wei M-T, Kriwacki
1190 RW & Brangwynne CP (2020) Composition-dependent thermodynamics of
1191 intracellular phase separation. *Nature* 581: 209–214

1192 Saha S, Weber CA, Nousch M, Adame-Arana O, Hoege C, Hein MY, Osborne Nishimura E,
1193 Mahamid J, Jahnel M, Jawerth L, *et al* (2016) Polar Positioning of Phase-Separated
1194 Liquid Compartments in Cells Regulated by an mRNA Competition Mechanism. *Cell*
1195 166: 1572-1584.e16

1196 Sanders DW, Kedersha N, Lee DSW, Strom AR, Drake V, Riback JA, Bracha D, Eeftens
1197 JM, Iwanicki A, Wang A, *et al* (2020) Competing Protein-RNA Interaction Networks
1198 Control Multiphase Intracellular Organization. *Cell* 181: 306-324.e28

1199 Smith J, Calidas D, Schmidt H, Lu T, Rasoloson D & Seydoux G (2016) Spatial patterning
1200 of P granules by RNA-induced phase separation of the intrinsically-disordered
1201 protein MEG-3. *eLife* 5: e21337

1202 Spike C, Meyer N, Racen E, Orsborn A, Kirchner J, Kuznicki K, Yee C, Bennett K & Strome
1203 S (2008a) Genetic analysis of the Caenorhabditis elegans GLH family of P-granule
1204 proteins. *Genetics* 178: 1973–1987

1205 Spike CA, Bader J, Reinke V & Strome S (2008b) DEPS-1 promotes P-granule assembly
1206 and RNA interference in C. elegans germ cells. *Development (Cambridge, England)*
1207 135: 983–993

1208 Strome S & Wood WB (1982) Immunofluorescence visualization of germ-line-specific
1209 cytoplasmic granules in embryos, larvae, and adults of Caenorhabditis elegans.
1210 *Proceedings of the National Academy of Sciences of the United States of America*
1211 79: 1558–1562

1212 Updike D & Strome S (2010) P granule assembly and function in Caenorhabditis elegans
1213 germ cells. *Journal of andrology* 31: 53–60

1214 Van Treeck B & Parker R (2018) Emerging Roles for Intermolecular RNA-RNA Interactions
1215 in RNP Assemblies. *Cell* 174: 791–802

1216 Wang JT, Smith J, Chen B-C, Schmidt H, Rasoloson D, Paix A, Lambrus BG, Calidas D,
1217 Betzig E & Seydoux G (2014) Regulation of RNA granule dynamics by
1218 phosphorylation of serine-rich, intrinsically disordered proteins in C. elegans. *eLife* 3:
1219 449–23

1220 Yang P, Mathieu C, Kolaitis R-M, Zhang P, Messing J, Yurtsever U, Yang Z, Wu J, Li Y,
1221 Pan Q, *et al* (2020) G3BP1 Is a Tunable Switch that Triggers Phase Separation to
1222 Assemble Stress Granules. *Cell* 181: 325-345.e28

1223 Yguerabide J, Schmidt JA & Yguerabide EE (1982) Lateral mobility in membranes as
1224 detected by fluorescence recovery after photobleaching. *Biophys J* 40: 69–75

1225 Zhang H, Elbaum-Garfinkle S, Langdon EM, Taylor N, Occhipinti P, Bridges AA,
1226 Brangwynne CP & Gladfelter AS (2015) RNA Controls PolyQ Protein Phase
1227 Transitions. *Molecular cell* 60: 220–230

1228

1229

1230 ## Supplementary Information

1231

1232 **Supplementary Figure 1**

1233

1234 SDS-PAGE of recombinantly-purified
1235 proteins used in this study. Four SDS-
1236 PAGE gels are shown (gel 1: lanes 1-13;
1237 gel 2: lanes 14-20; gel 3: lanes 21-23, gel
1238 4: lanes 24-26). Lane 21 is not adjacent
1239 to lanes 22 and 23 in gel 3; lanes 24, 25
1240 and 26 represent non-adjacent lanes in
1241 gel 4.

1242

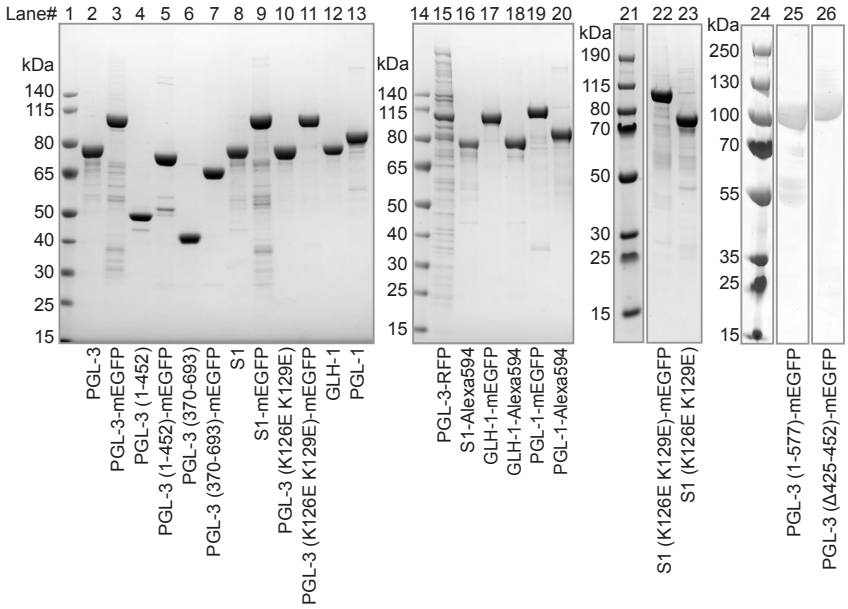

Supplementary Figure 2

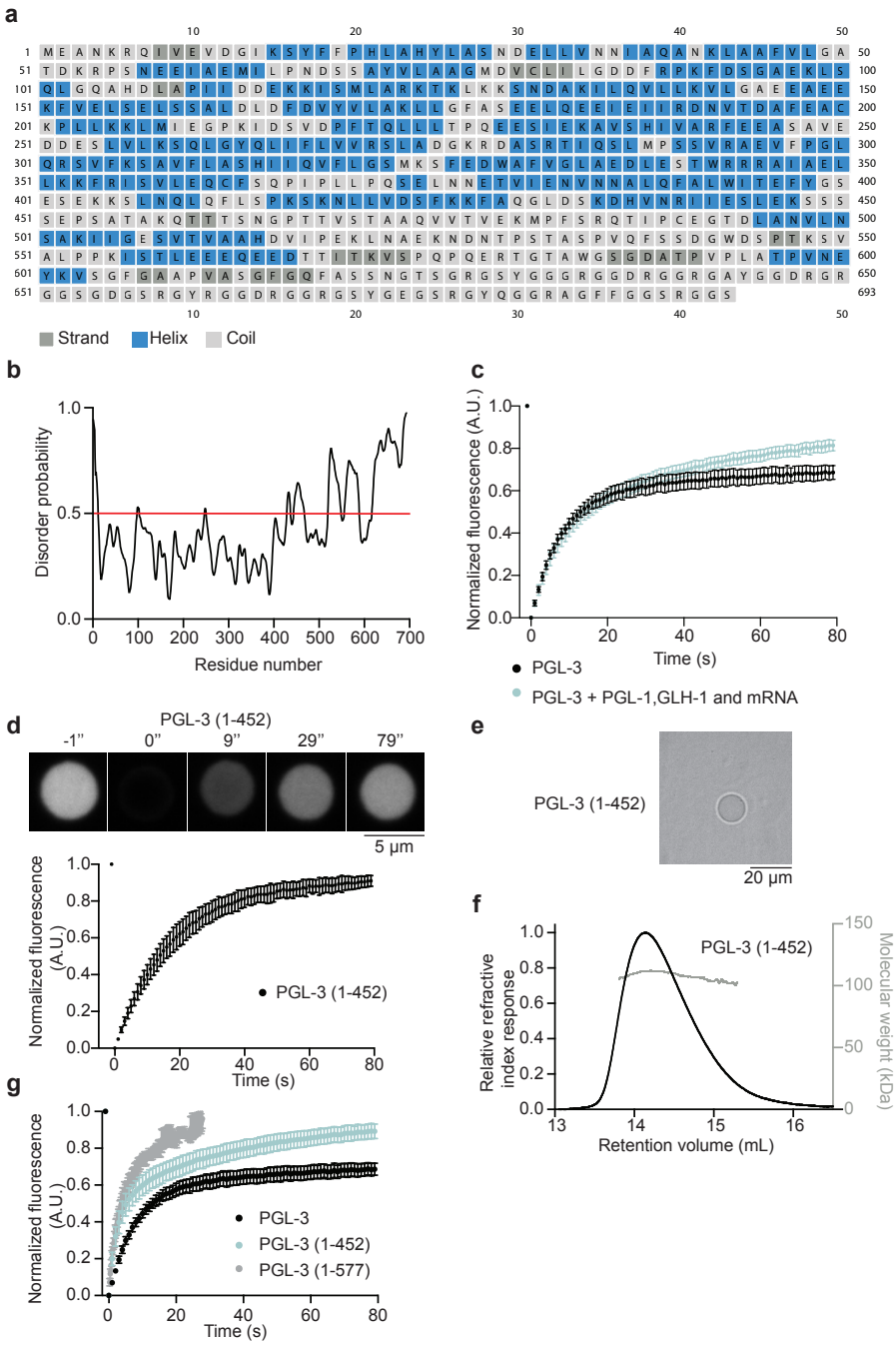

a Sequence of PGL-3 with secondary structure highlighted in different colors as predicted by the web-based PSIPRED 4.0 server. Dark grey β strand, blue: α helix, light grey: coil. (http://bioinf.cs.ucl.ac.uk/psipred/)
b Plot of disorder probability across the length of PGL-3, as predicted by the web-based PrDOS (Protein DisOrder prediction System) server with false-positive rate of 5.0% (http://bioinf.cs.ucl.ac.uk/psipred/).
c Plot of average normalized fluorescence over time in bleached regions (1.5 µm x 1.5 µm) within condensates of PGL-3 alone (black circles, 10 µM, 5% mEGFP-tagged, n = 18), or PGL-3 (blue circles, 5 µM, 5% mEGFP-tagged, n = 21) in presence of PGL-1 (6.7 µM), GLH-1 (1 µM) and total mRNA (14 ng/µL). Error bars represent 1 SD.
d Time-lapse fluorescence micrographs show fluorescence recovery over time after a condensate of PGL-3 (1-452) (5 µM, 5% mEGFP-tagged) was photobleached. Scale bar 5 µm. Below is shown a plot of average normalized fluorescence over time in 11 condensates of PGL-3 (1-452) (21 µM, 5% mEGFP-tagged) that were photobleached. Error bars represent 1 SD.
e Bright field micrograph of PGL-3 (1-452) (5 µM) in 25 mM HEPES pH 7.5, 100 mM KCl, 1 mM DTT. Scale bar 20 µm.
f Representative plot of size exclusion chromatography and multi-angle light scattering (SEC-MALS) data for PGL-3 (1-452). Black: relative refractive index response (Y-axis, left), Grey: molecular weight in kDa (Y- axis, right). Measurements were performed in 25 mM HEPES, 300 mM KCl, 1 mM TCEP. Average molecular weight of PGL-3 (1-452) estimated from SEC-MALS is 109.5 (±1.4) kDa (n = 2). Expected molecular weight based on amino acid sequence is 50.5 kDa, suggesting that PGL-3 (1-452) exists as a dimer.
g Plot of average normalized fluorescence over time in bleached regions (1.5 µm x 1.5 µm) within condensates of PGL-3 (black circles, 5% mEGFP-tagged, n = 18), PGL-3 (1-452) (blue circles, 5% mEGFP-tagged, n = 24) and PGL-3 (1-577)-mEGFP (grey circles, bleached region 1.4 µm x 1.4 µm, n = 8). Error bars represent 1 SD.

Supplementary Figure 3

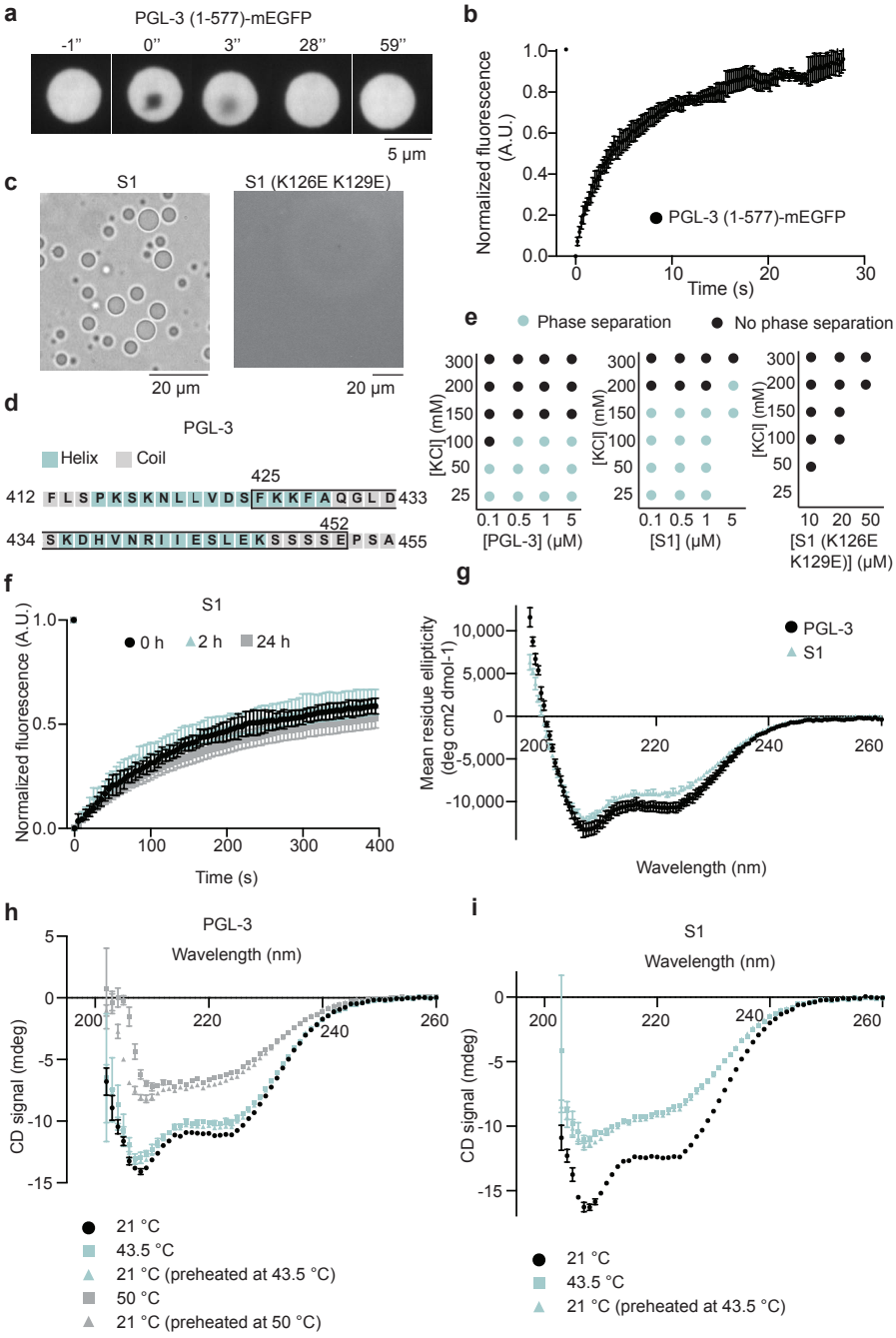

a Time-lapse fluorescence micrographs show fluorescence recovery over time after a 1.4 µm x 1.4 µm area within a condensate of PGL-3 (1-577)-mEGFP (20 µM) was photobleached. Scale bar 5 µm.
b Plot showing average normalized fluorescence of bleached region (1.4 µm x 1.4 µm) within PGL-3 (1-577)-mEGFP condensates (n=8) over time. Error bars represent 1 SD.
c Bright-field micrographs of S1 (8 µM) in 25 mM HEPES pH 7.5, 100 mM KCl, 1 mM DTT and S1 (K126E K129E) (50 µM) in 25 mM HEPES pH 7.5, 150 mM KCl, 1 mM DTT. Scale bar 20 µm.
d Sequence of PGL-3 (412-455) with secondary structure highlighted in different colors as predicted by the web-based PSIPRED 4.0 server. Light blue: α helix, grey: coil. (http://bioinf.cs.ucl.ac.uk/psipred/). Residues 425-452 (shuffled in S1) are highlighted within open black box.
e Phase diagrams of PGL-3, S1 and S1(K126E K129E) at different protein and salt (KCl) concentrations in 25 mM HEPES pH 7.5, 1 mM DTT. Blue circles represent conditions where phase separation was observed. Black circles represent conditions where phase separation was absent. 5% of the pool of protein was tagged with mEGFP in each case.
f Plot showing average normalized fluorescence of bleached regions (1.5 µm x 1.5 µm) within condensates of S1 (10 µM, 5% mEGFP-tagged) over time. Condensates were assayed at different times after assembly via phase separation and incubation at 20 °C (Black circles: immediately following assembly (n = 16), blue triangles: 2 h post-assembly (n = 14), grey squares: 24 h post-assembly (n = 11). Error bars represent 1 SD.
g Plot of mean residue ellipticity of PGL-3 and S1 vs. wavelength assayed using circular dichroism (CD) spectroscopy. Black circles: PGL-3 (3 µM, 10 mM Potassium phosphate pH 7.5, 300 mM KCl, 1 mM TCEP), Blue triangles: S1 (3 µM, 10 mM Potassium phosphate pH 7.5, 300 mM KCl, 1 mM TCEP). Error bars represent 1 SD among six CD scans.
h-i Plots of circular dichroism signal vs. wavelength of **h** PGL-3 (3 µM) and **i** S1 (3 µM) in 25 mM HEPES pH 7.5, 1 M KCl and 1 mM DTT at different temperatures. Error bars represent 1 SD among six CD scans. Black circles: 21 °C, blue squares: 43.5 °C, blue triangles: 21 °C (after preheating at 43.5 °C), grey squares: 50 °C, grey triangles: 21 °C (after preheating at 50 °C).

Supplementary Figure 4

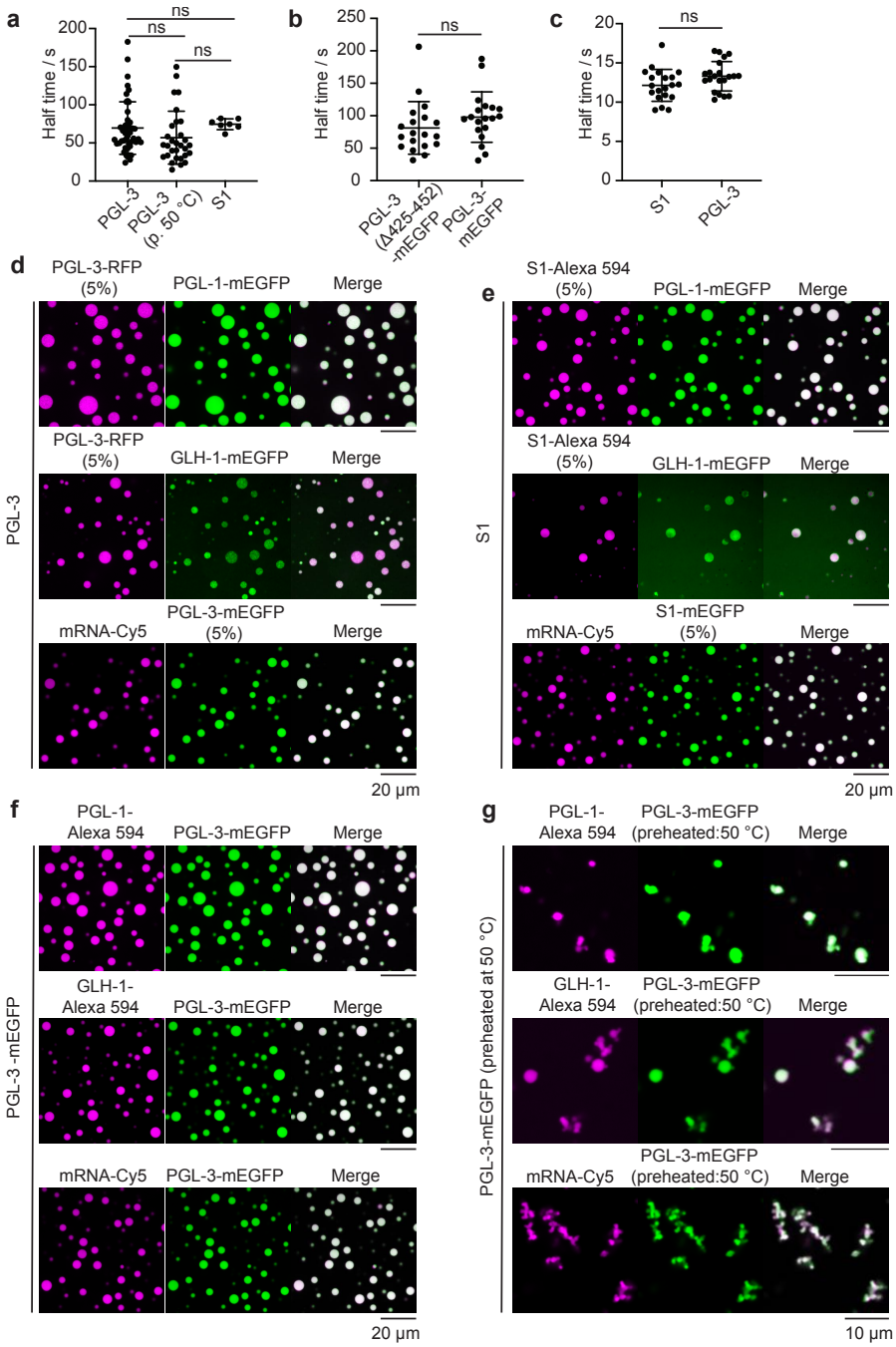

a-c Plots with estimated half times of recovery with statistical analysis for three experiments. Each black circle represents estimated half time (s) for one bleached P granule/condensate. The mean and 1 SD are also indicated. Half times were estimated by fitting the data points for normalized fluorescence signal for individual P granule/condensate to the equation: $F_t = (F_0 + F_\infty*(t/t_{1/2}))/(1 + t/t_{1/2})$. Only points with very confident fit (p<1E-11) were considered for the statistical analysis (described in more detail in Materials and Methods section). "ns" indicates no significant difference (p > 0.05) between the half times of recovery. Experiments were as following: **a** Bleaching of the P granules in live animals of N2 strain after PGL-3 (n = 46), preheated PGL-3 (n = 29) or S1 (n = 7) protein injection (Fig. 4b); One way ANOVA performed to compare the groups with following p values: p(PGL-3 vs. preheated PGL-3) = 0.241; p(PGL-3 vs. S1) = 0.926; p(preheated PGL-3 vs. S1) = 0.417 ; **b** Bleaching of the P granules in live animals in the strains expressing PGL-3 (Δ425-452)-mEGFP (n = 19) or PGL-3-mEGFP (n = 19) (Fig. 4b). T test performed to compare the two groups with resulting p value p = 0.205 **c** Bleaching of the condensates of PGL-3 (5 µM) (n=21) or S1 (5 µM) (n=20). 5% of the pool of protein was tagged with mEGFP) in presence of PGL-1 (6.7 µM), GLH-1 (1 µM), and total mRNA (14 ng/µL). T test performed to compare the two groups with resulting p value p = 0.104 **d-g** Fluorescence micrographs show concentration of PGL-1, GLH-1 and act-4 mRNA (in vitro transcribed) within condensates of PGL-3 **d**, S1 **e**, PGL-3-mGFP **f** and PGL-3-mEGFP preheated at 50 °C **g**. To track condensates of PGL-3 and S1 in **d-e**, 5% of the pool of PGL-3 or S1 proteins used were tagged with RFP, mEGFP or Alexa 594. Fluorophores used to track PGL-1 (mEGFP or Alexa 594), GLH-1 (mEGFP or Alexa 594), and mRNA (Cy5) are specified in each case. Scale bars **d-f** 20 µm, **g** 10 µm.

Supplementary Figure 5

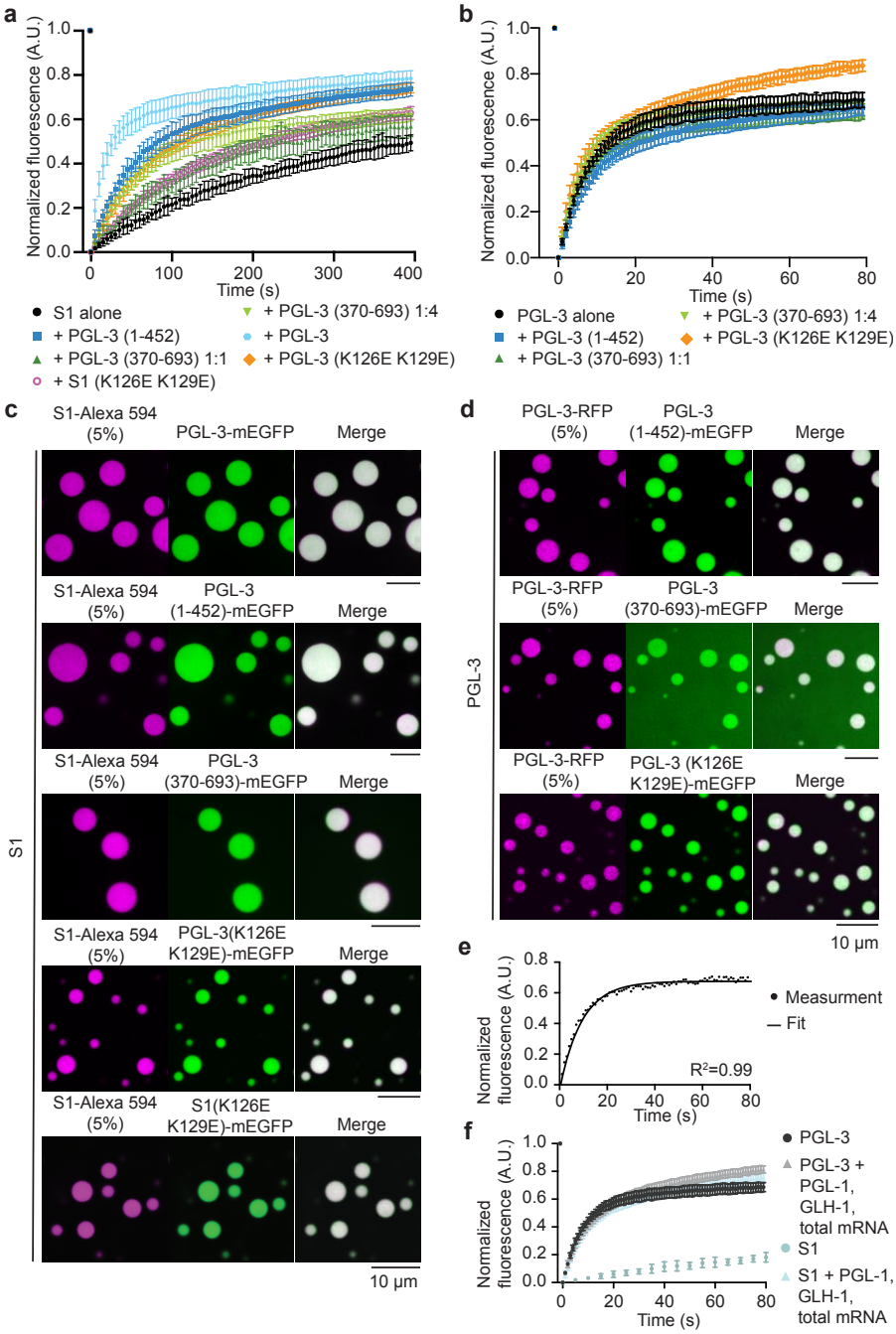

a Plot of average normalized S1-mEGFP fluorescence over time in bleached regions (1.5 µm x 1.5 µm) within the condensates of defined composition as follows. Black circles: S1 alone (10 µM, 5% mEGFP-tagged) (n = 18), light green triangle: S1 (5 µM, 5% mEGFP-tagged) + PGL-3 (370-693) (20 µM) (n = 24), blue square: S1 (5 µM, 5% mEGFP-tagged) + PGL-3 (1-452) (5 µM) (n = 16), light blue hexagon: S1 (5 µM, 5% mEGFP-tagged) + PGL-3 (5 µM) (n = 20), green triangle: S1 (5 µM, 5% mEGFP-tagged) + PGL-3 (370-693) (5 µM) (n = 11), orange diamond: S1 (5 µM, 5% mEGFP-tagged) + PGL-3 (K126E K129E) (5 µM) (n = 17), magenta open circle: S1 (5 µM, 5% mEGFP-tagged) + S1 (K126E K129E) (5 µM) (n = 13). Error bars represent 1 SD.

b Plot of average normalized PGL-3-mEGFP fluorescence over time in bleached regions (1.5 µm x 1.5 µm) within the condensates of defined composition as follows. Black circles: PGL-3 alone (10 µM, 5% mEGFP-tagged) (n = 18), light green triangle: PGL-3 (5 µM, 5% mEGFP-tagged) + PGL-3 (370-693) (20 µM) (n = 12), blue square: PGL-3 (5 µM, 5% mEGFP-tagged) + PGL-3 (1-452) (5 µM) (n = 28), green triangle: PGL-3 (5 µM, 5% mEGFP-tagged) + PGL-3 (370-693) (5 µM) (n = 13), orange diamond: PGL-3 (5 µM, 5% mEGFP-tagged) + PGL-3 (K126E K129E) (5 µM) (n =12). Error bars represent 1 SD.

c-d Fluorescence micrographs show concentration of PGL-3-mEGFP, PGL-3 (1-452)-mEGFP, PGL-3 (370-693)-mEGFP, PGL-3 (K126E K129E)-mEGFP or S1(K126E K129E)-mEGFP within condensates of S1 **c** or PGL-3 **d**. To track condensates of S1 and PGL-3 in **c-d**, 5% of the pool of S1 or PGL-3 proteins used were tagged with Alexa 594 or RFP. Scale bar 10 µm.

e A representative plot of normalized PGL-3-mEGFP fluorescence over time in bleached regions (1.5 µm x 1.5 µm) within a condensate and corresponding single exponential fit. FRAP data was fitted to the single exponential function: $y = a * (1 - \exp(-b*x))$. R^2 values were ≥ 0.92 for all fits.

f Plot of average normalized fluorescence over time in bleached regions (1.5 µm x 1.5 µm) within condensates of PGL-3 alone (black circles, 10 µM, 5% mEGFP-tagged, n = 18), PGL-3 in presence of PGL-1 (6.7 µM), GLH-1 (1 µM) and total mRNA (14 ng/µL) (grey triangles, 5 µM, 5% mEGFP-tagged, n = 21), S1 alone (blue circle, 10 µM, 5% mEGFP-tagged, n =18), or S1 in presence of PGL-1 (6.7 µM), GLH-1 (1 µM) and total mRNA (14 ng/µL) (light blue triangle, 5 µM, 5% mEGFP-tagged, n = 21). Error bars represent 1 SD.

Supplementary Figure 6

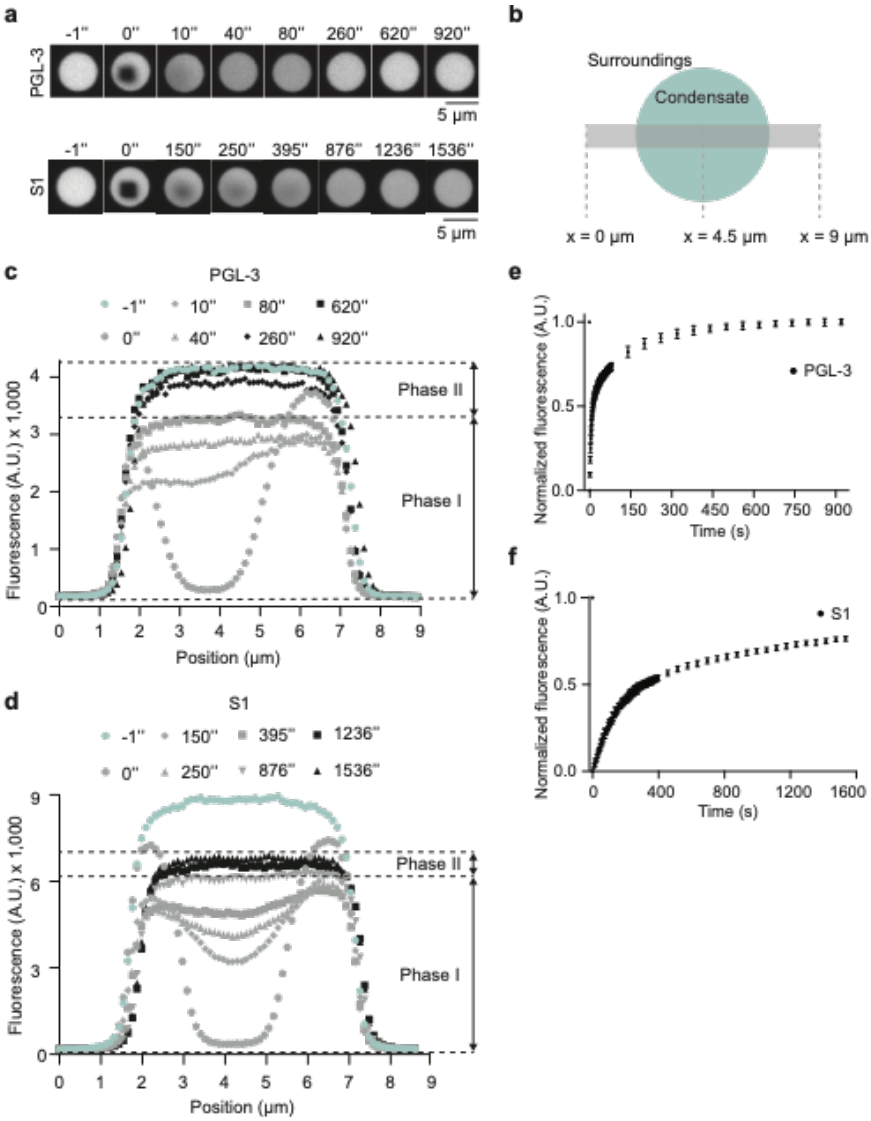

a Time-lapse fluorescence micrographs show fluorescence recovery after photobleaching over time in condensates of PGL-3 (10 µM) or S1 (10 µM) (5% of the pool of protein was tagged with mEGFP). Scale bars 5 µm.
b Cartoon defining position with respect to a condensate. This position scheme was used to generate fluorescence-profile plots shown in **c** and **d**.
c-d Profile plots mapping the fluorescence signal at different positions within a condensate of PGL-3 **c** or S1 **d**. Plots shows fluorescence signal in selected area (see **b** at different time points. Over time, fluorescence recovers within bleached regions through a combination of internal rearrangement of molecules within condensates and exchange of molecules between condensates and surroundings. Colors represent different recovery phases: blue for time before bleaching, grey for phase I and black for phase II. Phase I is a fast phase of fluorescence recovery that promotes homogenization of fluorescence signal within the condensate predominantly via internal rearrangement of molecules. Phase II is a slower phase of fluorescence recovery that depend predominantly on additional replenishment of unbleached molecules from the surroundings. Different time points are shown as follows. **c** Blue circle: -1 s (before bleaching), grey circle: 0 s (moment of bleaching), grey diamond: 10 s, grey triangle: 40 s, grey square: 80 s, black diamond: 260 s, black square: 620 s, black triangle: 920 s after bleaching. **d** Blue circle: -1 s (before bleaching), grey circle: 0 s (moment of bleaching), grey diamond: 150 s, grey triangle: 250 s, grey square: 395 s, grey reverse triangle: 876 s, black square: 1236 s, black triangle: 1536 s after bleaching.
e-f Plots of average normalized fluorescence over time in bleached regions (1.5 µm x 1.5 µm) within the condensates of PGL-3 (n = 9) **e** or S1 (n=9) **f** imaged as described in **a**. Error bars represent 1 SD.

Supplementary Movies

Supplementary Movie 1
Time-lapse fluorescence micrographs show fluorescence recovery after photobleaching of P granules in live *C. elegans* (pachytene region) expressing PGL-3-mEGFP. Time stamp and scale bar (3 µm) indicated (related to Fig. 4e).
Supplementary Movie 2
Time-lapse fluorescence micrographs show fluorescence recovery after photobleaching of P granules in live *C. elegans* (pachytene region) expressing PGL-3 (Δ425-452)-mEGFP. Time stamp and scale bar (3 µm) indicated (related to Fig. 4e).